Nano Research

Open Access

Review Article

Electrospun nanofibers for electrochemical reduction of CO_2: From spinning fabrication techniques to electrocatalyst design

Yanbiao Liu[1,3], Ping Feng[2] ✉, Zhenzhen Wang[3], Yan Yan[3], Yong Zheng[4], Yu Zhang[5], and Mingkai Liu[3] ✉

[1] *Key Laboratory of Ministry of Education on Safe Mining of Deep Metal Mines, Northeastern University, Shenyang 110004, China*
[2] *Institute for Technical Chemistry and Environmental Chemistry, Friedrich-Schiller-Universität Jena, Jena 07743, Germany*
[3] *School of Chemistry & Chemical Engineering, Anhui University of Technology, Ma'anshan 243002, China*
[4] *College of Materials and Chemical Engineering, Key Laboratory of inorganic Nonmetallic Crystalline and Energy Conversion Materials, China Three Gorges University, Yichang 443002, China*
[5] *School of Mechanical and Power Engineering, East China University of Science and Technology, Shanghai 200237, China*

Cite this article: *Nano Research*, **2025**, *18*, 94907154. https://doi.org/10.26599/NR.2025.94907154

ABSTRACT: Electrochemical reduction of CO_2 (ECO_2RR) into value-added fuels and chemicals presents a promising avenue for mitigating CO_2 emissions while simultaneously contributing to economic growth, thereby addressing critical environmental and energy challenges. However, the large-scale implementation of ECO_2RR is significantly impeded by the necessity to design efficient catalysts that exhibit both high activity and selectivity. These catalysts must overcome the sluggish kinetics associated with ECO_2RR as well as the competing hydrogen evolution reaction. In recent decades, electrospun nanofibers have garnered considerable attention as potential catalysts for ECO_2RR, attributable to their high surface area with abundant active sites, tunable functionalities, and enhanced selectivity. This review comprehensively examines the rational design of ECO_2RR catalysts utilizing electrospinning technology. We commence with an in-depth exploration of the principles underlying the electrospinning process and subsequently summarize key factors influencing this process, including solution parameters, environmental conditions, and electrospinning operational parameters. Moreover, we discuss recent advancements in ECO_2RR catalysts synthesized through electrospinning, encompassing carbon nanofibers, composite nanofibers, and metal nanofibers. Finally, we delineate future perspectives and the challenges that electrospun materials face in the context of ECO_2RR applications. This review aims to inspire high-quality research directed toward the advancement of electrospun materials for improved performance in ECO_2RR.

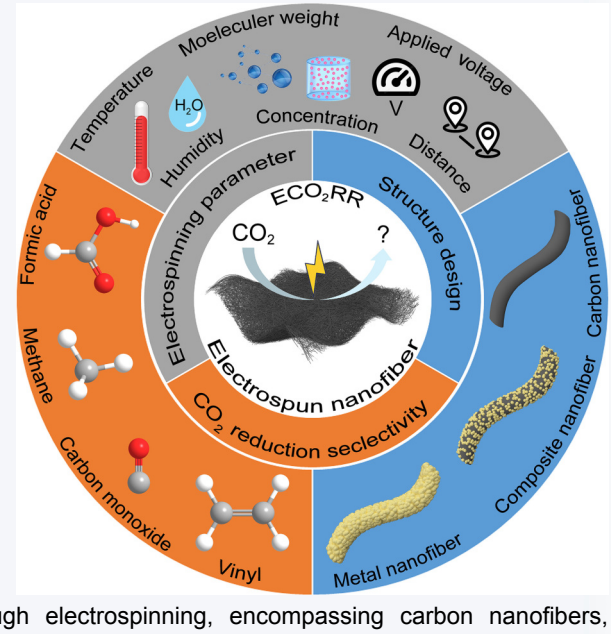

KEYWORDS: CO_2 reduction reaction, catalyst design, electrospinning, single-atom catalysts

1 Introduction

The atmospheric concentration of carbon dioxide (CO_2) has risen sharply since the industrial revolution due to the large-scale use of fossil fuels [1–5]. This increase has led to significant environmental risks, including global warming, rising sea levels, ocean acidification, and more frequent extreme weather events [6–10]. It has been reported that atmospheric CO_2 levels have surged dramatically, rising from below 280 ppm in the 1760s to over 415 ppm today [11–13]. To reduce dependence on fossil fuels, there has been growing interest in renewable energy sources such as solar, wind, and hydropower [14–16]. Advances in harnessing technologies have led to a substantial decrease in the cost of green electricity and a significant increase in production [17–20]. However, the intermittent nature of electricity generated from

Received: November 4, 2024; **Revised:** November 21, 2024
Accepted: November 24, 2024

✉Address correspondence to Ping Feng, ping.feng@helmholtz-berlin.de; Mingkai Liu, liumingkai@ahut.edu.cn

renewable sources poses challenges for its integration into the electrical power grid [21, 22]. Alternatively, green electricity can be utilized to produce various raw chemicals through electrocatalytic processes, such as the electrochemical CO_2 reduction reaction (ECO_2RR) [23–29]. In this process, electrons serve as reductive agents, typically in conjunction with a proton source like water (H_2O) [30]. The ECO_2RR can be conducted at ambient temperature and pressure, provided that electricity is supplied [31–36]. The reduction products, including carbon monoxide (CO), formate (HCOOH), methanol, methane (CH_4), ethylene (C_2H_4), and ethanol, are valuable raw chemicals and fuels [37–40]. Consequently, the advancement of ECO_2RR is expected to mitigate the CO_2 emission and contribute to economic growth, addressing environmental and energy problems [41–44].

Although ECO_2RR technology holds significant promise, several challenges hinder its widespread implementation and efficiency [45–48]. The chemical inertness of CO_2, stemming from its symmetrical linear structure and strong C=O bonds (with a bond energy of 750 $kJ{\cdot}mol^{-1}$), creates substantial barriers to the electrochemical process, resulting in a high activation energy [49–51]. Furthermore, the ECO_2RR involves intricate multi-electron and multi-proton transfer mechanisms, which produce a variety of reaction intermediates [52–54]. Developing ideal catalysts that exhibit high activity, stability, and cost-effectiveness for efficient ECO_2RR is urgently needed [55–60]. Side reactions such as the hydrogen evolution reaction (HER) can become significant at both low and high potentials. This is because the thermodynamic requirements for CO_2 reduction are similar to those for HER. In practice, ECO_2RR demands a higher energy input than the theoretical minimum. This discrepancy allows HER to proceed more easily, thereby reducing the overall energy efficiency of the electroreduction system [17, 61–63].

In recent years, significant efforts have been dedicated to developing catalysts with high efficiency and selectivity, leading to notable advancements in the field [64–66]. Among these catalysts, carbon nanofibers (CNFs) have emerged as a up-and-coming class of electrocatalysts for ECO_2RR, attracting substantial attention [67–69]. CNFs offer several unique advantages in ECO_2RR: (1) Their exceptional porosity and surface area enhance the exposure of active sites and facilitate rapid mass transportation. (2) The electronic properties of CNFs can be precisely tuned through metal doping or functionalization, which affects the reaction pathways for ECO_2RR. (3) The polymer nanofiber could work as attractive precursors or templates to fabricate numerous metal nanofibers (such as metal alloy nanofibers and metal oxide nanofibers) as electrocatalysts for selective ECO_2RR. Among various nanofiber synthesis methods, such as melt spinning [70], phase separation [71], and template-based synthesis [72], electrospinning is recognized as a convenient, versatile, and cost-effective technique for synthesizing nanofibers with a high surface area-to-volume ratio, controllable dimensions, tunable functionalities, lightweight characteristics, and high porosity [73–75]. Recently, hydrophobized electrospun nanofibers with hierarchical porosity have been developed via electrospinning and employed as integral gas diffusion electrodes (GDEs) for full-pH CO_2 electroreduction. The optimized GDE achieved near-unity Faradaic efficiency (FE) for CO production and demonstrated stable operation for over 273 h, with a total energy efficiency of 38% in a neutral membrane electrode setup. Additionally, it exhibited a high single-pass CO_2 conversion rate of 78% in an acidic membrane configuration. These results pave the way for industrial-scale CO_2 electrolysis through innovative GDE design [76].

For the past few years, CNFs and their functional derivatives have made notable advancements in the field of ECO_2RR [77]. Although a limited review exists in this field, providing an updated perspective on their application in ECO_2RR is both timely and necessary given the rapid advancements in this area. Furthermore, the influence of key factors on electrospinning, which are critical for the successful synthesis of nanofibers and the rational design of nanofiber structures for ECO_2RR, has not been discussed in the existing review [78]. This review begins by highlighting the distinctive characteristics of electrospinning, followed by a detailed discussion of its principles. Key factors that influence the electrospinning process, such as solution parameters, environmental parameters, and process parameters, are summarized. We then reviewed the recent advancements in electrospun nanofibers as catalysts for ECO_2RR toward different products from the perspective of materials design strategies such as carbon nanofiber, composite nanofiber (carbon nanofiber with metal species), and metal nanofibers, as shown in Fig. 1. Finally, the challenges ahead and future perspectives are discussed.

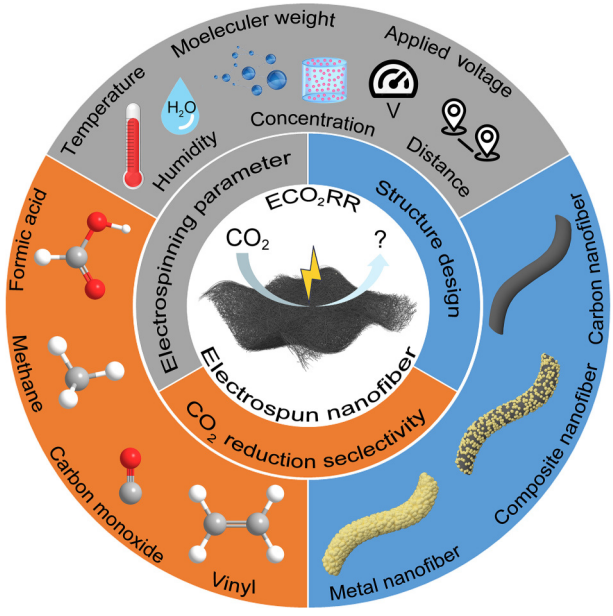

Figure 1 Schematic diagram of CNFs and their derivatives for ECO_2RR.

2 Overview of electrospinning

2.1 History for electrospinning

The development of electrospinning spans over a century, with contributions from various scientists and engineers who discovered and refined the basic principles behind the process. The early prototype of electrospinning goes back to the 1700s when electrostatic atomization was developed. This process shares similar physics with electrospinning, where an applied electrostatic field counteracts surface tension to increase the liquid body's surface area [79]. In the early foundations, from the late 19th century to the early 20th century, people began to discover the phenomenon of electrostatic spinning and tried to use it to produce fibers. In 1897, Lord Rayleigh laid the theoretical groundwork for electrospinning

by studying the behavior of fluid droplets subjected to electrostatic forces [80]. His work on the instability of charged liquid jets, later known as "Rayleigh instability", became essential for understanding the process of jet formation in electrospinning. In 1902, Cooley [81] and Morton [82] each filed patents on the electrical dispersion of fluids through electrospraying, a process based on the same fundamental principles as electrospinning.

Formhals made significant contributions to the practical development of electrospinning [83]. He filed a series of patents in the 1930s and 1940s, describing machines and methods for producing polymer fibers using electrostatic forces. His designs focused on producing textile fibers from cellulose acetate, marking one of the earliest commercial applications of the electrospinning process [84]. Research into electrospinning was reignited in the mid-20th century when scientists began investigating its potential for producing ultrafine fibers (now called nanofibers). Different polymers have been explored for electrospinning, and the understanding of electrospinning parameters, including electric field strength and solvent properties, has been refined. The development of electrospinning theory progressed slowly over time. Taylor initially provided a critical theoretical explanation for jet formation during electrospinning [85]. By applying a mathematical model to describe the shape of a fluid droplet influenced by electrostatic forces, he derived the voltage balance equation for the Taylor cone and calculated that its stable angle is 49.3°, now known as the "Taylor cone", which was experimentally verified later [86].

The growing interest in nanotechnology and the need for materials with high surface area-to-volume ratios led to a resurgence of research into electrospinning [87]. Electrospinning has been explored to produce nanofibers for various high-tech applications, such as filtration, drug delivery, and tissue engineering [88, 89]. Reneker and Chun published a pivotal paper in 1995 that sparked renewed interest in electrospinning [90]. They demonstrated how electrospinning could create polymer nanofibers with diameters as small as a few nanometers, highlighting the potential applications in materials science and medicine. Throughout the 2000s, electrospinning gained significant interest from both the scientific community and industry [91, 92]. As one of the fast-moving fields, researchers developed more sophisticated electrospinning techniques, including co-axial, tri-axial, centrifugal, corona, bubble, rotary metals (cylinder, disk, and ball), high-speed, and three-dimensional (3D) electrospinning to produce composite nanofibers with specific properties [93]. In recent years, the number of publications on electrospinning has increased year by year and has gained broad interest in the field of ECO_2RR.

2.2 Principle for electrospinning

The fundamental principle of electrospinning involves utilizing electrostatic forces to stretch and extrude a polymer solution or melt into ultrafine fibers (Fig. 2(a)). The process begins with dissolving a polymer in an appropriate solvent or melting it. The resulting solution or melt must possess specific viscosity, surface tension, and conductivity for stable fiber formation during electrospinning. Initially, a pendant droplet forms on the spinneret due to the liquid's surface tension. A high-voltage power supply is then activated to create an electric field between the polymer solution in a syringe and a grounded collector, typically ranging from 5 to 30 kV, depending on the materials and configuration used. As the voltage increases, the electrostatic forces surpass the surface tension at the syringe tip, forming a cone-shaped structure known as a "Taylor cone". When the electric field exceeds a critical threshold, a fine jet of polymer solution is emitted from the tip of the Taylor cone (Fig. 2(b)). The critical voltage V_c for electrospinning is described by the following expression derived from Taylor's calculation [93]

$$V_c^2 = (4H^2/h^2)\left[\ln(2h/R) - 1.5\right](1.3\pi R\gamma) \times 0.09 \quad (1)$$

Here, H, h, R, and γ denote the distance from the spinneret tip to the collector, the length of the liquid column, the inner radius of the spinneret, and the surface tension of the spinning solution, respectively. A factor of 0.09 is incorporated to estimate the voltage. As the jet moves toward the collector, it experiences stretching and thinning due to electrostatic repulsion. Concurrently, the solvent evaporates or the melt cools, leading to the formation of solidified fibers. These fibers are then deposited onto the grounded collector, forming either a non-woven mesh or aligned fibers, depending on the specific setup. Electrospinning is a straightforward and highly versatile technique, with a key advantage being its ability to produce one-dimensional (1D) nanostructured materials, including polymer nanofibers, metal oxide nanofibers, CNFs and their composites (Fig. 2(c)).

The transition from jet to fiber formation is highly complex. Although the actual spinning process occurs within a few milliseconds, extensive studies have shown that the jet's path is intricate, including significant bending, whipping, and stretching motions that ultimately lead to the formation of the final fiber. Yarin et al. [94, 95] observed the jet path with a high-speed camera and analyzed the bending instability during flight. Through a combination of experimental and modeling studies, they discovered that the typical trajectory of the jet involves an initial straight segment followed by a series of coils with progressively larger diameters (Fig. 2(d)). The formation of a spiraling coil with an expanding diameter is caused by bending instability, which results from the repulsive forces between charged segments of the jet. Furthermore, additional bending instabilities may emerge on the existing curved coil, forming smaller spirals that wrap around the path of the primary coil (Fig. 2(e)). This phenomenon persists in a repetitive coil pattern until the solvent evaporates, at which the solidified polymer prevents any further elongation. Zhang et al. categorized this process into five key stages: (i) the formation of a Taylor cone under the influence of an electrostatic field; (ii) the attainment of a critical voltage leading to the ejection of the jet; (iii) the stable straight-line extension of the charged jet; (iv) the onset of whipping instability, which thins the jet in the electric field; and (v) the evaporation of the solvent, resulting in solid fiber formation and subsequent collection [96]. Moreover, the electrospinning process is influenced by various factors, including solution parameters, process conditions, and environmental variables, which significantly impact the quality of the resulting fibers. A comprehensive discussion of these factors will be provided in the subsequent sections.

Electrospun nanofibers produced from electrospinning exhibit a wide range of unique properties that are absent in their bulk counterparts [83]. These properties result from their high specific surface area, large surface-to-volume ratio, and significant fiber length-to-diameter aspect ratio. Consequently, electrospun nanofibers display enhanced reaction rates per unit mass due to unique quantum effects, high electrical conductivity, and favorable redox potentials [97]. Furthermore, these attributes facilitate the formation of highly porous structures with adjustable pore sizes and

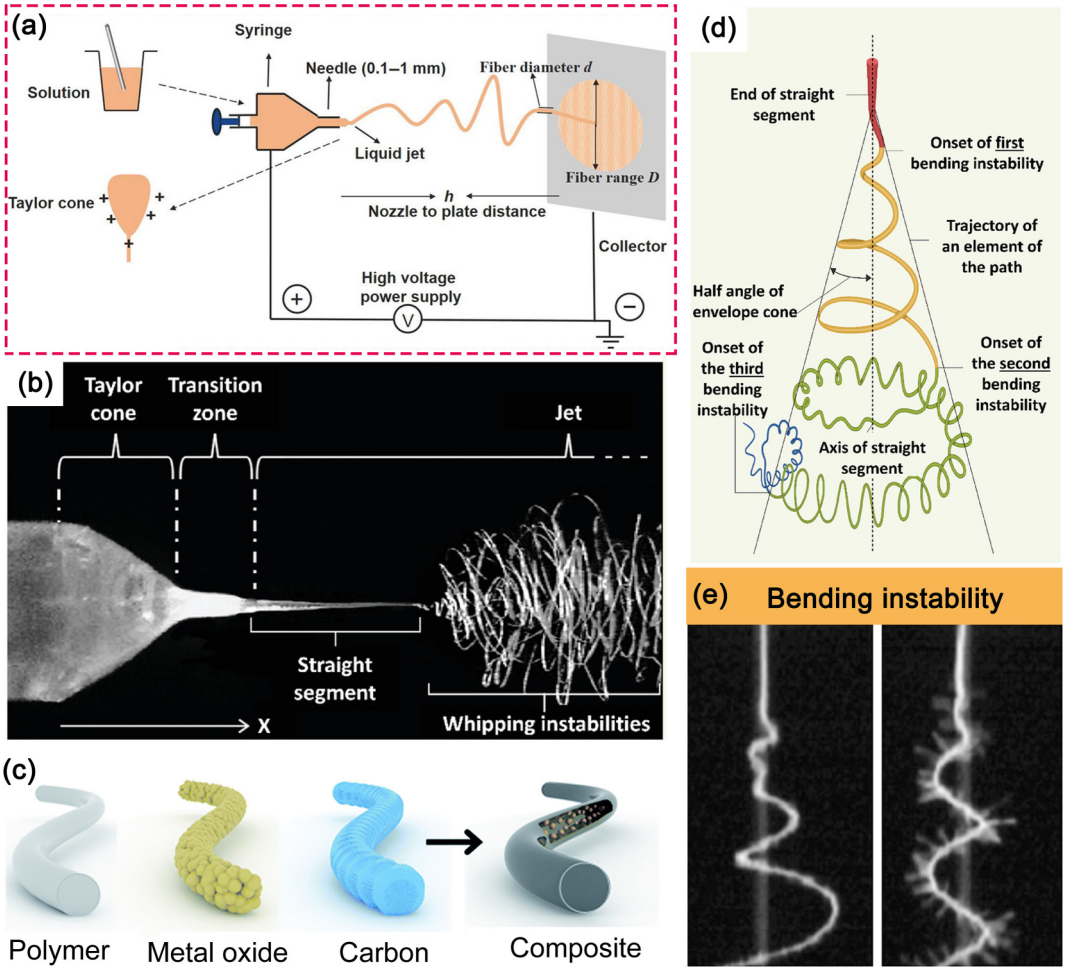

Figure 2 (a) Basic illustration of the electrospinning setup. Reproduced with permission from Ref. [99], © WILEY-VCH Verlag GmbH & Co. KGaA, Weinheim 2020. (b) High-speed photograph outlining the Taylor cone formation, the linear segment of the polymer jet, and the whipping jet region. Reproduced with permission from Ref. [83], © Keirouz, A. et al. 2023. (c) Diverse electrospun nanofibers are obtained by controlling various parameters such as precursor, calcination atmosphere, and the type of nozzle. Reproduced with permission from Ref. [100], © The Royal Society of Chemistry 2016. (d) The prototypical instantaneous position of the jet path succeeding through the three sequential bending instabilities. Reproduced with permission from Ref. [83], © Keirouz, A. et al. 2023. (e) Branches on the electrical bending coils of a jet of polycaprolactone dissolved in acetone. Reproduced with permission from Ref. [95], © Elsevier Ltd. 2008.

large surface area, enabling efficient chemical functionalization [98]. As a result of these advantages, electrospun nanofibers are extensively utilized in the design and synthesis of highly efficient electrocatalysts for ECO_2RR.

3 Factors influencing the nanofiber formation

The formation of nanofibers by electrospinning is influenced by several critical factors, which can be categorized into solution parameters, processing parameters, and environmental conditions. Understanding and optimizing these factors are essential for achieving desired nanofiber properties, including diameter, uniformity, and mechanical strength. Adjustments to each parameter can lead to significant changes in fiber morphology and functionality, making it critical for researchers to fine-tune the electrospinning process for specific applications.

3.1 Environment parameters

3.1.1 Temperature

The temperature affects the diameter of nanofibers through two opposing mechanisms: (i) It increases solvent evaporation, and (ii) it decreases solution viscosity. As the temperature rises, the viscosity of the polymer solution generally decreases, enhancing the solution's flow ability and facilitating the formation of continuous jets. However, if the viscosity drops too much, the polymer jet may become unstable, forming droplets or beaded fibers. Additionally, higher temperatures speed up solvent evaporation during electrospinning, leading to faster fiber solidification. Nevertheless, excessively rapid evaporation may cause defects, such as incomplete fiber formation or irregular diameters. In general, higher temperatures tend to produce fibers with smaller diameters, as observed by Vrieze et al. in their study using cellulose acetate (CA) and poly(vinylpyrrolidone) (PVP) for electrospinning (Fig. 3(a)) [101].

3.1.2 Humidity

Humidity affects nanofibers' diameter by influencing the solidification process of the charged jet. However, this effect depends on the chemical properties of the polymer (Fig. 3(b)) [102]. When water or hydrophilic solvents, such as ethanol, are involved, increased humidity has been shown to delay solvent

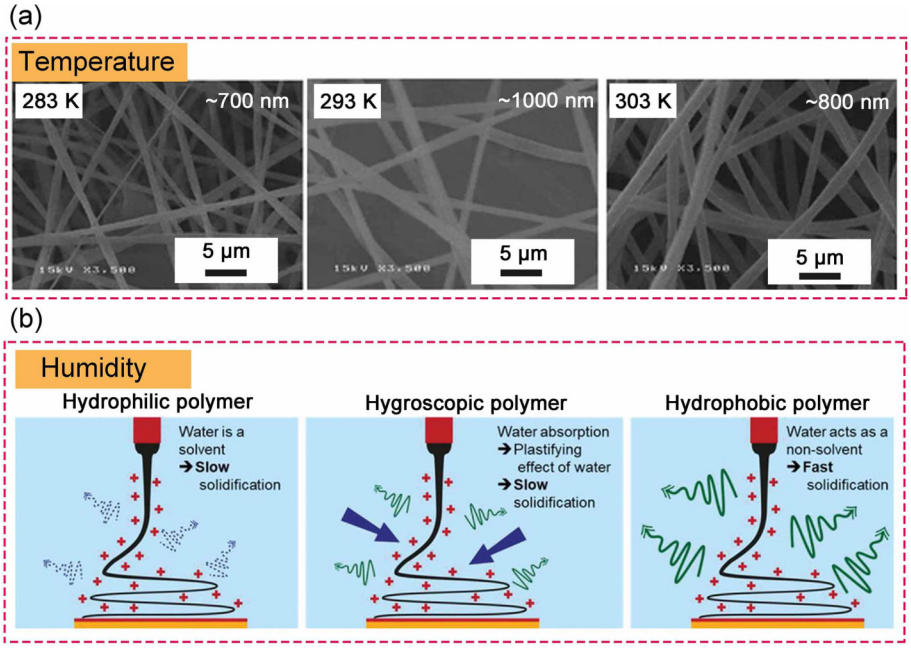

Figure 3 (a) Scanning electron microscopy (SEM) images of the PVP (10%) nanofibers at different temperatures (283, 293, and 303 K). Reproduced with permission from Ref. [101], © Springer Science+Business Media, LLC 2008. (b) Effects of humidity on the solidification rate of the electrospinning jet as a function of the polymer hydrophilicity. Reproduced with permission from Ref. [103], © Wiley-VCH GmbH 2021.

evaporation, thereby postponing the solidification of fibers and reducing the diameter of nanofibers [103]. S. De Vrieze et al. [101] reported that the average diameter of polyvinylpyrrolidone nanofibers decreased from approximately 900 to 600 nm as humidity increased from 20% to 45%. This finding aligns with the observations of Tripatanasuwan et al., who noted a similar reduction in the average diameter of poly(ethylene oxide) (PEO) nanofibers with increasing humidity [104]. Unlike Tripatanasuwan et al., S. De Vrieze et al. did not use water as the solvent. The evaporation rate of ethanol remains constant across different relative humidity levels at the same temperature. Nevertheless, the absorption of surrounding moisture impacts the solidification rate of the nanofibers, allowing for extended jet elongation, which leads to thinner nanofibers. In hydrophobic polymer systems, water absorption in the jet induces early solidification through precipitation, leading to thicker nanofibers at higher humidity. Sung et al. [105] reported that the diameter of polystyrene nanofibers (hydrophobic) increased gradually from 130 to 380 nm as the relative humidity rose from 10% to 70%.

3.2 Solution parameters

3.2.1 *Concentration*

Variations in the concentration of the polymer solution affect the uniaxial stretching of the charged jet during the electrospinning process. For instance, at low concentrations of the polymer solution, the applied electric field and surface tension can cause entangled polymer chains to fragment before reaching the collector, resulting in the formation of beads or beaded nanofibers. As the concentration increases, the viscosity rises, enhancing the chain entanglement and enabling the polymer chains to overcome the surface tension, which leads to the production of uniform and bead-free electrospun nanofibers. However, if the concentration exceeds a critical threshold, it can obstruct the flow of the solution through the needle tip. This blockage may cause the polymer solution to dry at the tip of the metallic needle, resulting in defective or beaded nanofibers. The morphologies of the beads exhibit a notable transition from a rounded droplet-like shape (in low-viscosity solutions) to an elongated droplet or ellipse, and ultimately to smooth fibers as viscosity increases [106].

3.2.2 *Conductivity*

The conductivity of the polymer solution affects the stretching and formation of nanofibers. Higher conductivity increases the charge density within the solution, enhancing electrostatic forces that stretch the charged jet, leading to improved fiber quality, such as fewer beads and thinner fiber diameters [107]. However, if the conductivity is too low, the electrostatic forces may be insufficient to overcome surface tension and viscoelastic resistance, preventing the continuous stretching of the liquid jet [108]. Using highly conductive solvents (e.g., acetone, chloroform, and ethyl acetate) or adding salts or electrolytes has enhanced the uniformity of electrospun fibers by minimizing bead formation and reducing fiber diameter [107].

3.2.3 *Viscosity*

The viscosity of the polymer solution is influenced by the polymer's molecular weight and concentration, which can affect the behavior of the electrospinning jet and the resulting fiber morphology. In a low-viscosity solution, the reduced entanglement between polymer chains limits jet stretching, leading to the fragmentation of the charged droplets into numerous tiny mists. As the viscosity increases, these mist particles begin to merge, causing the bead shapes in the fibers to shift from spherical to spindle-like, ultimately resulting in the formation of smooth fibers (Figs. 4(a)–4(e)) [99]. At an even higher viscosity, the charged jet cannot achieve sufficient stretching and refinement, producing larger fiber diameters with a broader diameter distribution.

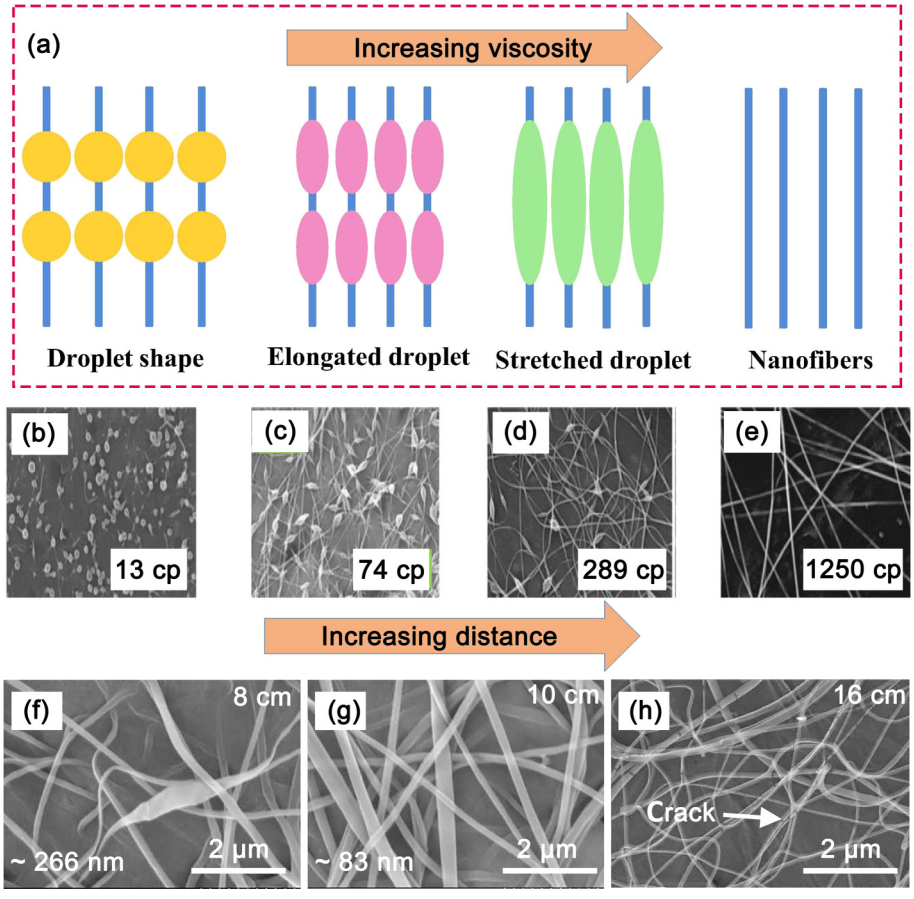

Figure 4 (a) Schematic variation and ((b)–(e)) SEM images of the morphology of electrospun PEO nanofibers with viscosity. Reproduced with permission from Ref. [102], © Production and hosting by Elsevier B.V. on behalf of King Saud University 2015. SEM images of 10 wt.% PVA nanofibers at working distance of (f) 8, (g) 10, and (h) 16 cm. Reproduced with permission from Ref. [110], © WILEY-VCH Verlag GmbH & Co. KGaA, Weinheim 2010.

3.2.4 *Molecular weight*

In general, a higher molecular weight polymer dissolved in a solvent will exhibit higher viscosity compared to the same polymer with a lower molecular weight. This occurs because the increased entanglement of polymer chains in the solution is essential for sustaining a continuous jet during electrospinning. These chain entanglements are crucial to stabilizing the jet, preventing droplet formation, and influencing the morphology of the resulting nanofibers, whether they form as beads or smooth fibers [109]. For successful electrospinning, the solution must contain a polymer with sufficient molecular weight and adequate viscosity to facilitate fiber formation.

3.3 Electrospinning parameters

3.3.1 *Tip-to-collector distance*

The tip-to-collector distance plays a significant role in influencing the jet path and the time the polymer jet spends traveling before it reaches the collector. As the polymer jet moves through the electric field, it is stretched by electrostatic forces, during which the solvent evaporates, allowing the jet to solidify and maintain its morphology. It has been reported that increasing the distance between the tip and the collector can reduce fiber diameter due to the greater stretching distance available [109]. However, if the applied voltage remains constant, the electric field strength decreases as the tip-to-collector distance increases, eventually leading to thicker fibers due to the weaker field. Guo et al. evaluated the effect of tip-to-collector distance on the morphology of electrospun polyvinyl alcohol (PVA) nanofibers under constant voltage [110]. They found that increasing the distance from 8 to 10 cm resulted in thinner fibers (from 266 to 93 nm). However, further increasing the distance to 16 cm led to decreased fiber uniformity and cracks in the fibers, as the electrostatic force became insufficient to counter the mechanical stress of stretching (Figs. 4(f)–4(h)).

3.3.2 *Applied voltage*

The applied voltage affects both the charge density of the solution and the strength of the electric field between the needle and the collector. An increase in voltage accelerates the electrospinning jet, drawing a larger volume of solution from the needle tip. If the solution feed rate remains constant, this can lead to a smaller and less stable Taylor cone [89]. Without considering the feed rate, higher voltage generally enhances the stretching of the solution, resulting in thinner fibers [111]. However, surpassing a certain voltage threshold can destabilize the process, leading to the formation of more beads on the fibers [112].

4 ECO_2RR fundamentals

ECO_2RR typically occurs in an electrochemical cell where CO_2 is reduced at the cathode while water or hydrogen is oxidized at the anode. The first prototype for CO_2 reduction dates back to 1887 when CO_2 was electrochemically converted to formic acid using a

mercury electrode as the cathode in an aqueous electrolyte [113]. In a breakthrough discovery in 1986, Hori and colleagues demonstrated that metallic copper could catalyze the conversion of CO_2 into hydrocarbons such as CH_4 and C_2H_4 [114]. Since then, copper and its derived catalysts have become the most extensively studied materials for ECO_2RR, as copper remains the only material capable of achieving high yields of hydrocarbon products. With the rapid development of material synthesis methods and nanotechnology, significant progress has been achieved in catalysts for ECO_2RR, including metal catalysts, non-metal catalysts, and metal-oxide and hybrid catalysts.

The ECO_2RR mechanism involves several key steps: (i) CO_2 is adsorbed onto the surface of the catalyst, leading to the formation of $*CO_2$ (* represents the active site) at the surface of the catalysts. This step poses significant thermodynamic challenges due to the strong bonding energies associated with the carbon–oxygen double bond [115]. (ii) CO_2 undergoes multiple proton-coupled electron transfer (PCET) processes to form intermediates such as *COOH, *OCHO, or *CO. (iii) Depending on the pathway, the reaction intermediates are further reduced to produce C_1 (CO, CH_3OH, CH_4, etc.) to C_{2+} products (including multi-carbon hydrocarbons and oxygenates, etc.) (Fig. 5). Within the context of the C_1 pathway, HCOOH is one of the primary liquid products generated through a two-electron reduction process. Typically, $*CO_2^-$ binds to the catalyst surface through two oxygen atoms, forming the *OCHO intermediate, from which HCOOH is preferentially produced via a proton-coupled electron transfer step. The formation of *CO is crucial for generating C_2 product, and the reaction pathways involving *CO intermediates, whether through multiple CPET or other steps, determine the final C_2 products. Cu-based materials have been identified as the most efficient catalysts, demonstrating significant selectivity and Faradaic efficiency for C_2 products. On the Cu (100) surface, *CO dimerization occurs before protonation at low overpotential and serves as the rate-determining step for the formation of C_2H_4, CH_3CH_2OH, and $CH_3CH_2CH_2OH$ [116].

The pH and applied potential are critical factors that directly impact the reactivity and selectivity of the ECO_2RR, resulting in various reduction products [117]. Side reactions such as the HER can become significant at both low and high potentials. This is because the thermodynamic requirements for CO_2 reduction are similar to those for HER. In practice, ECO_2RR demands a higher energy input than the theoretical minimum. This discrepancy allows HER to proceed more easily, thereby reducing the overall energy efficiency of the electroreduction system. Furthermore, the CO_2 reduction process involves multiple intermediates that can strongly influence the reaction pathways and final products [118]. The selectivity of ECO_2RR is predominantly determined by the binding affinities of key intermediates (e.g., *COOH, *OCHO, and *CO) on the surface of the electrocatalyst.

5 Electrospun nanofibers as the ECO_2RR catalysts

5.1 Carbon nanofibers

CNFs have received extensive attention in ECO_2RR due to their unique properties such as good electrical conductivity, large specific surface area, and adjustable structure. However, traditional CNFs

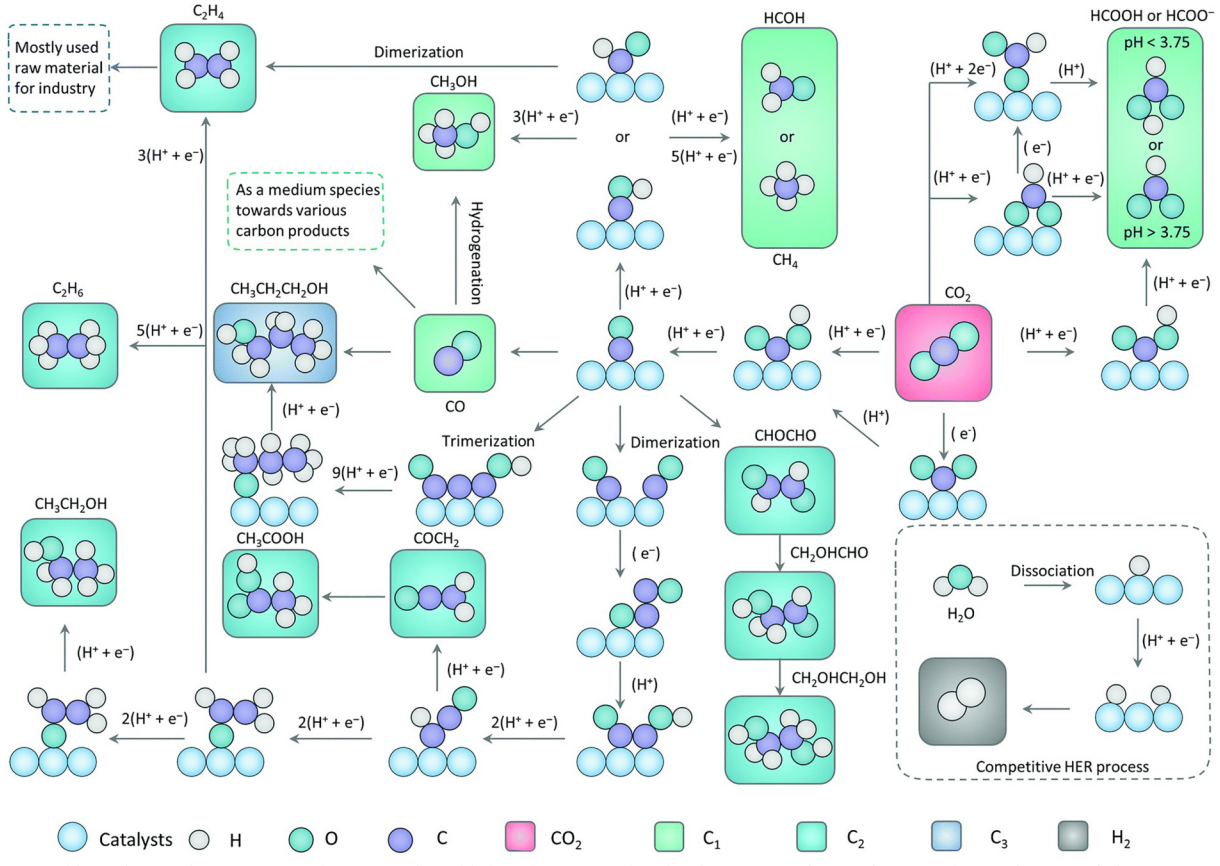

Figure 5 Possible roadmaps of ECO_2RR towards various value-added products. Reproduced with permission from Ref. [17], © The Royal Society of Chemistry 2022.

still have certain limitations in catalytic performance. Therefore, how to improve the catalytic performance of CNFs for ECO_2RR by regulating their structure has become a research hotspot.

In some studies, pore structure is regulated by introducing pore-forming agents during the preparation process of carbon materials. Chuai et al. prepared a carbon film electrode embedded with Ni single-atom (SA)-modified nitrogen-doped carbon nanofiber (Ni-N_x-C) through electrospinning and pyrolysis methods [119]. During the preparation process, potassium chloride is selected as a pore-forming agent to adjust the porous structure of the carbon film. At the same time, electrochemical tests were conducted in an H-cell to evaluate the performance of the Ni-N_x-C catalyst. It was found that the optimized porous carbon film electrode ($K_{0.66}$Ni-NC) has a CO Faradaic efficiency (FE_{CO}) exceeding 90% within a wide potential range of −0.8–−1.6 V vs. reversible hydrogen electrode (RHE) (Fig. 6(a)). Moreover, in a 30 h durability test, it can still maintain more than 90% FE_{CO} at −0.8 V vs. RHE (Fig. 6(b)). This indicates that the porous structure facilitates the mass transfer of CO_2 and increases the exposure degree of active sites during the ECO_2RR process. A simple and scalable method was developed to prepare self-supporting carbon film electrodes, avoiding the stability problems caused by using polymer binders in traditional powder catalysts. By adjusting the porous structure of the carbon film, the ECO_2RR performance of the electrode is significantly improved. However, further in-depth research is still needed for the reaction mechanism of ECO_2RR, especially in terms of how the porous structure specifically affects electron transfer and intermediate adsorption during the reaction process.

Another method to regulate pore structure is to adjust the size of through-holes in carbon nanofibers by controlling the pre-oxidation process. For example, by adjusting the pre-oxidation heating rate, different multi-channel hollow structures with abundant mesopores can be formed inside the carbon nanofiber [120]. Taking SnN-HF-5 as an example, it has a uniform diameter and a clear multi-channel structure, with an internal channel diameter of about 70 nm (Fig. 6(c)). This unique structure enhances the adsorption capacity of CO_2, significantly contributing to the current density for CO_2 reduction in the potential range of 0.4–0.8 V vs. RHE, and having a high FE_{CO} at 0.47 V vs. RHE (Fig. 6(d)). This is because the appropriate through-hole size and multi-channel structure are beneficial for the diffusion and adsorption of CO_2 inside the carbon nanofiber, providing more contact opportunities for the reaction and thereby improving the catalytic performance. At the same time, element doping is another effective method to regulate the structure of carbon materials. The doping of Sn and N changes the electronic structure of carbon materials, which is beneficial for the adsorption and activation of CO_2 and then affects the reaction path of ECO_2RR. SnN-HFs with abundant mesopores and controllable multi-channel hollow structures are prepared by electrospinning technology. Elemental doping to modulate the carbon structure plays a crucial role in enhancing catalytic performance, enabling carbon nanofibers to achieve high FE_{CO} and increased current density at specific potentials. This is because doping changes the electron cloud distribution of carbon materials, enhancing its adsorption capacity for CO_2 molecules. At the same time, it may also affect the stability of reaction intermediates and promote the reaction to generate target products. The research mainly focuses on the Sn-N co-doped system and the effects of doping with other elements or different doping combinations on the performance of ECO_2RR have not been involved. The accuracy and universality of the established reaction mechanism model may need further verification and improvement.

Combining active site modification with structure regulation is an effective strategy to further improve catalytic performance. The role of single-atom active sites and how to better expose and utilize these sites can be further explored. Wang et al. used electrospinning technology and took polymethyl methacrylate (PMMA) as a pore-forming agent to prepare a self-supporting porous carbon nanofiber electrode modified with atomically dispersed nickel active sites (Ni-PCNF) (Fig. 6(e)) [121]. As a gas diffusion electrode, Ni-PCNF achieved a FE_{CO} of 98.6% in an H-cell (Fig. 6(f)). In addition to modifying active sites, optimizing pore distribution is also essential. Using PMMA to adjust pore distribution and form a vertically aligned porous structure is beneficial for the adsorption and mass

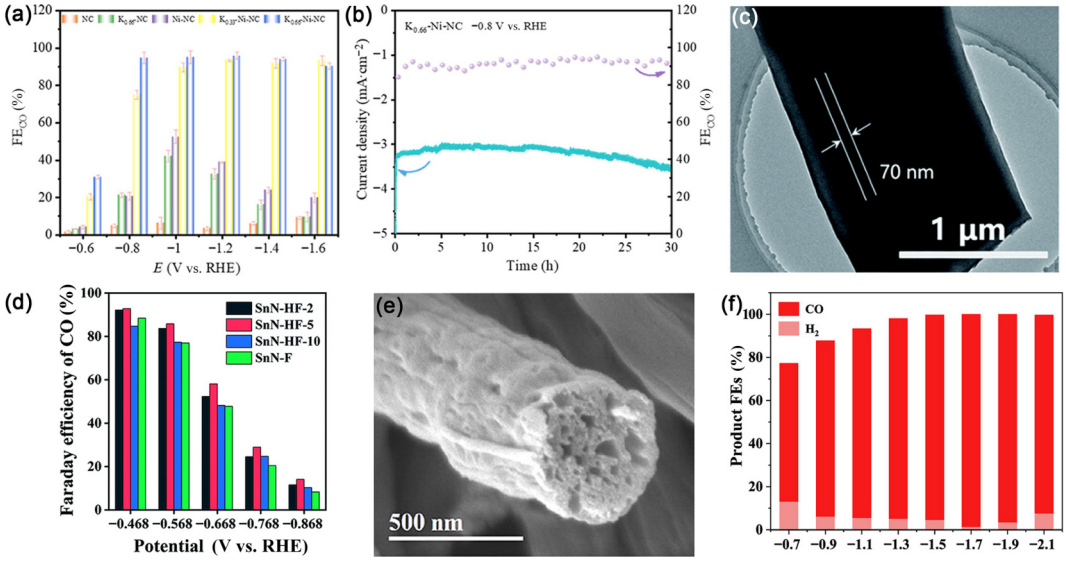

Figure 6 (a) Faradaic efficiencies of the CO. (b) Durability tests of the $K_{0.66}$-Ni-NC for 30 h at −1.0 V vs. RHE in the H-cell (0.1 M $KHCO_3$). Reproduced with permission from Ref. [119], © American Chemical Society 2024. (c) Transmission electron microscopy (TEM) image of the SnN-HF-5. (d) Faradaic efficiency of CO formation for Sn/N-CNFs at −0.468–−0.868 V (vs. RHE). Reproduced with permission from Ref. [120], © The Royal Society of Chemistry 2021. (e) SEM image of the Ni-PCNF-0.5PMMA. (f) FEs of all products of Ni-PCNF-0.5PMMA in the H-cell. Reproduced with permission from Ref. [121], © American Chemical Society 2022.

transfer of CO_2. The single nickel catalyst effectively converts CO_2 into CO. By adjusting the content of PMMA, the pore structure of the electrode can be effectively controlled, thereby optimizing its ECO_2RR performance. Although certain tests have been conducted for the stability of the electrode during long-term operation, further in-depth research is still needed on factors that may affect stability, such as the structural evolution of carbon nanofibers and the long-term activity of nickel atoms.

Single-atom catalysts (SACs) have attracted significant interest in the field of ECO_2RR due to their high activity and selectivity. Supported on CNFs, SACs offer multiple advantages. By altering the central metal atom, the adjacent coordinating elements, and the coordination number, the electronic structure and catalytic performance of the CNFs can be effectively modulated [122, 123]. In a recent study, researchers reported on the fabrication of polyvinylidene fluoride (PVDF) nanofiber membranes enriched with Fe^{3+} ions using the electrospinning technique (Fig. 7(a)) [124]. These membranes were further processed through defluorination crosslinking to create a robust scaffold structure. The study revealed that Fe^{3+} ions within the nitrogen-doped porous carbon fiber membrane catalyst (Fe-N-CF) were present as SAs, establishing a stable Fe-N_4-C coordination environment (Fig. 7(b)). This configuration played a crucial role in enhancing the catalytic performance of the material. When evaluated in a 0.5 M $NaHCO_3$ at −0.51 V vs. RHE, the Fe-N-CF catalyst demonstrated an impressive FE_{CO} of 97%, showcasing its high selectivity towards the reduction of CO_2 to CO (Fig. 7(c)). The Fe-N-CF catalyst also exhibited excellent durability for ECO_2RR (13 h) (Fig. 7(d)). Furthermore, density functional theory (DFT) calculations demonstrated that the Fe-N-CF catalyst substantially lowered the energy barriers associated with the formation of the intermediate *COOH and the subsequent desorption of CO (Fig. 7(e)). In another study, the use of zeolitic imidazolate framework-8 (ZIF-8) as a template for assisted pyrolysis led to the successful synthesis of tin-nitrogen doped porous carbon nanofibers (Sn/NCNFs) [125]. The Sn/NCNFs catalyst, benefiting from the porous fibrous morphology and a large number of exposed Sn-N active sites (Fig. 7(f)), demonstrated a FE_{CO} as high as 96.5% and a low Tafel slope of 68.8 mV·dec^{-1} (Figs. 7(g) and 7(h)).

5.2 Composite nanofibers (carbon nanofibers with metal species) as the ECO_2RR catalyst

The ECO_2RR presents a complex challenge due to the ability to produce a diverse array of C_1 products, each following distinct reaction pathways. This diversity complicates the precise manipulation and enhancement of the reaction process. A choice of metal species is a pivotal factor in directing the conversion of CO_2 towards specific C_1 products (such as HCOOH, CO, and CH_4). Leveraging electrospinning techniques, the incorporation of metal salts into the spinning solution facilitates the creation of CNFs catalysts, which are intricately embedded with metal nanoparticles or isolated metal atoms [126–128]. These metal species serve as active sites, effectively lowering the activation energy necessary for CO_2 reduction and augmenting the reaction rate. Significantly, this

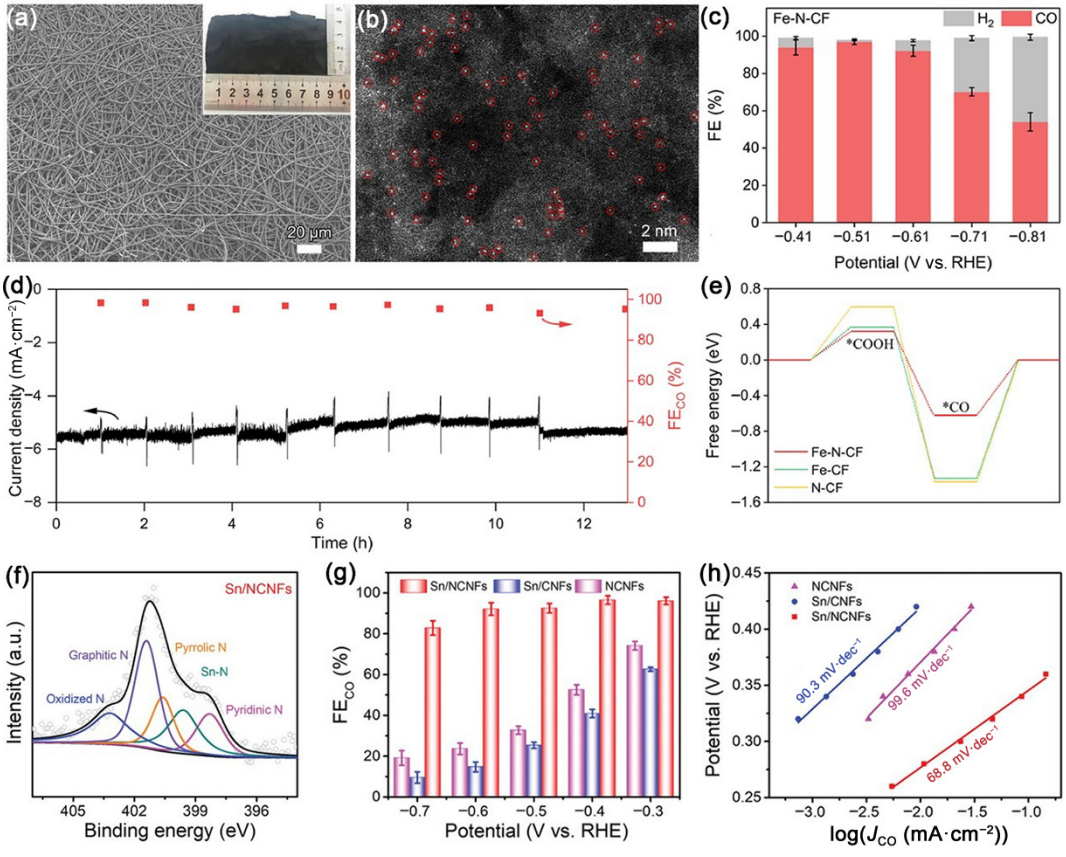

Figure 7 (a) and (b) SEM image images of Fe-N-CF. (c) Faradaic efficiency of CO product in ECO_2RR on Fe-N-CF at various cathode potentials. (d) Stability test of Fe-N-CF at −0.51 V vs. RHE. (e) Free energy for CO on Fe-N-CF. Reproduced with permission from Ref. [124], © Elsevier B.V. 2024. (f) High-resolution N 1s X-ray photoelectron spectroscopy (XPS) spectrum of the Sn/NCNFs. (g) FE_{CO} of Sn/NCNFs at different potentials in a flow cell. (h) Tafel slopes of Sn/NCNFs. Reproduced with permission from Ref. [125], © Wiley-VCH GmbH 2022.

approach allows for an extensive range of metal species to be integrated, both in terms of type and quantity, which greatly amplifies the selectivity for the production of the desired C_1 products [129, 130].

5.2.1 HCOOH

HCOOH, a prominent C_1 compound, has become a focal point in chemical safety due to its potential for hydrogen storage applications [131–133]. The latest research reveals that the efficiency of ECO_2RR can be significantly amplified by the strategic design of catalysts, with particular emphasis on tin (Sn), bismuth (Bi), and indium (In)-based nanomaterials.

Sn-based catalysts are extensively utilized in the study of ECO_2RR for formate production. Notably, the oxidation state of tin exhibits excellent selectivity for formate. Zhang et al. employed electrospinning to fabricate a tin dioxide hollow nanotube (SnO_2 HNT) with a sophisticated three-dimensional cross-linked network (Figs. 8(a) and 8(b)) [134]. This nanostructure substantially boosts the catalyst's specific surface area and significantly increases the density of active sites. Such features greatly enhance the mass transfer dynamics and modify the electronic structure, which are crucial for catalytic activity. Remarkably, the SnO_2 HNTs demonstrated a FE of 87.4% for producing of C_1 products at an electrode potential of −1.1 V vs. RHE. Furthermore, at this potential, the SnO_2 HNTs achieved an impressive FE_{HCOOH} of 75.0%, a figure markedly superior to that of conventional SnO_2 nanoparticles (Fig. 8(c)). This research underscores the potential of meticulously tailoring the electronic and geometric attributes of metal oxides to significantly uplift the efficiency of ECO_2RR.

In-based compounds, such as In_2O_3, exhibit exceptional selectivity for formate production in the ECO_2RR. By reducing the energy barrier for the formation of the key intermediate $HCOO^-$, they effectively facilitate the generation of formate. For instance, a heterostructure of GaN and In_2O_3 encapsulated porous carbon nanofibers was constructed via electrospinning and the phase transition of eutectic gallium-indium during calcination, denoted as GaN/In_2O_3@PCNF (Fig. 8(d)) [135]. The GaN/In_2O_3@PCNF heterostructure catalyst exhibited a maximum FE_{HCOOH} of 87% (Fig. 8(e)) in a 0.5 M $KHCO_3$ solution, with a maximum partial current density of 29.7 mA·cm^{-2} (Fig. 8(f)), and demonstrated prolonged durability (Fig. 8(g)). This remarkable activity is attributed to the rich defect structure and interactions between GaN and In_2O_3, which may reduce electron transfer resistance and accelerate the electron transfer to CO_2 molecules.

Owing to their abundant reserves and environmental benignity, Bi-based catalysts are also commonly utilized in ECO_2RR. These Bi-based catalysts exhibit excellent selectivity for formate production in the ECO_2RR. The bismuth-loaded, nitrogen-doped, and porous carbon nanofibers (Bi@PCNF-500) catalyst was fabricated by electrospinning and subsequent thermal treatment (Fig. 9(a)) [136]. The presence of the nitrogen-doped porous carbon matrix modulates the surface charge density, promotes electron delocalization, and facilitates the formation of favorable intermediates, thereby enhancing catalytic performance. Results indicate that Bi@PCNF exhibits a FE_{HCOOH} of 94.9% (Fig. 9(b)) and maintains excellent catalytic stability over 12 h in a flow cell (Fig. 9(c)). The integration of metal catalysts with carbon supports

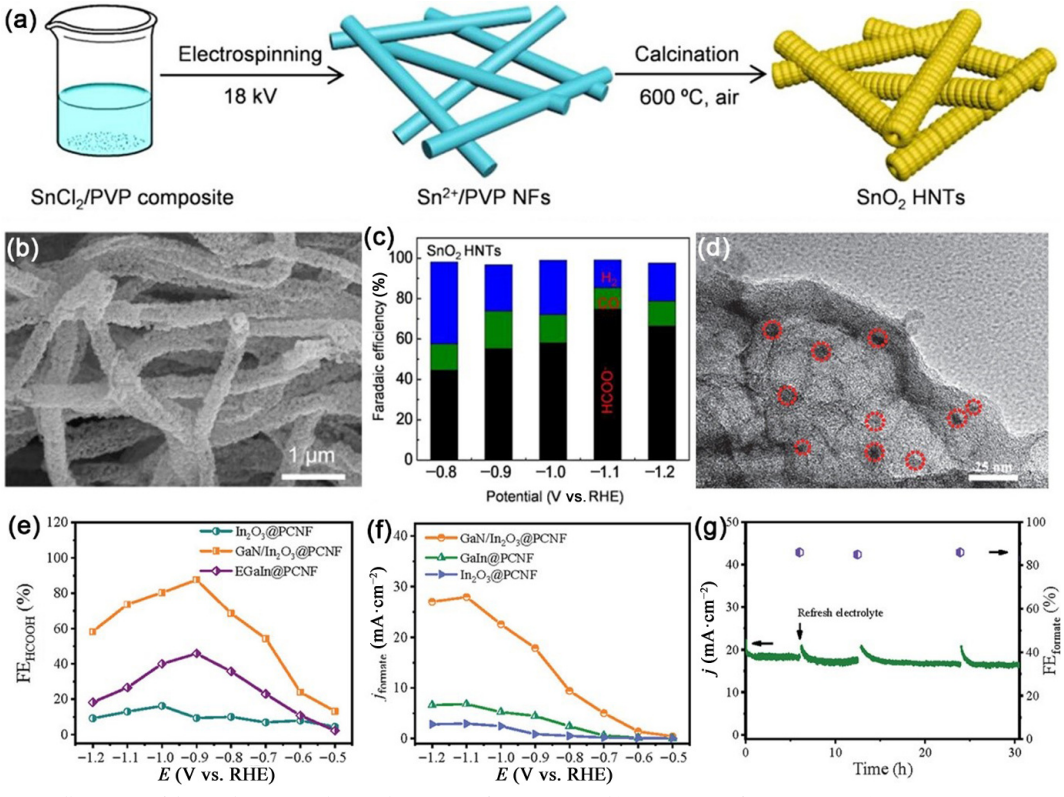

Figure 8 (a) Schematic illustration of the synthetic procedure and structure of SnO_2 HNTs. (b) SEM image of SnO_2 HNTs. (c) SnO_2 HNTs in ECO_2RR under different applied voltages. Reproduced with permission from Ref. [134], © American Chemical Society 2023. (d) High-magnification TEM image of the GaN/In_2O_3@PCNF. (e) Faradaic efficiency of formate for GaN/In_2O_3@PCNF at different applied potentials. (f) Partial current density of formate for GaN/In_2O_3@PCNF at different potentials. (g) Durability test and FE of formate for GaN/In_2O_3@PCNF. Reproduced with permission from Ref. [135], © Dalian Institute of Chemical Physics, the Chinese Academy of Sciences 2023.

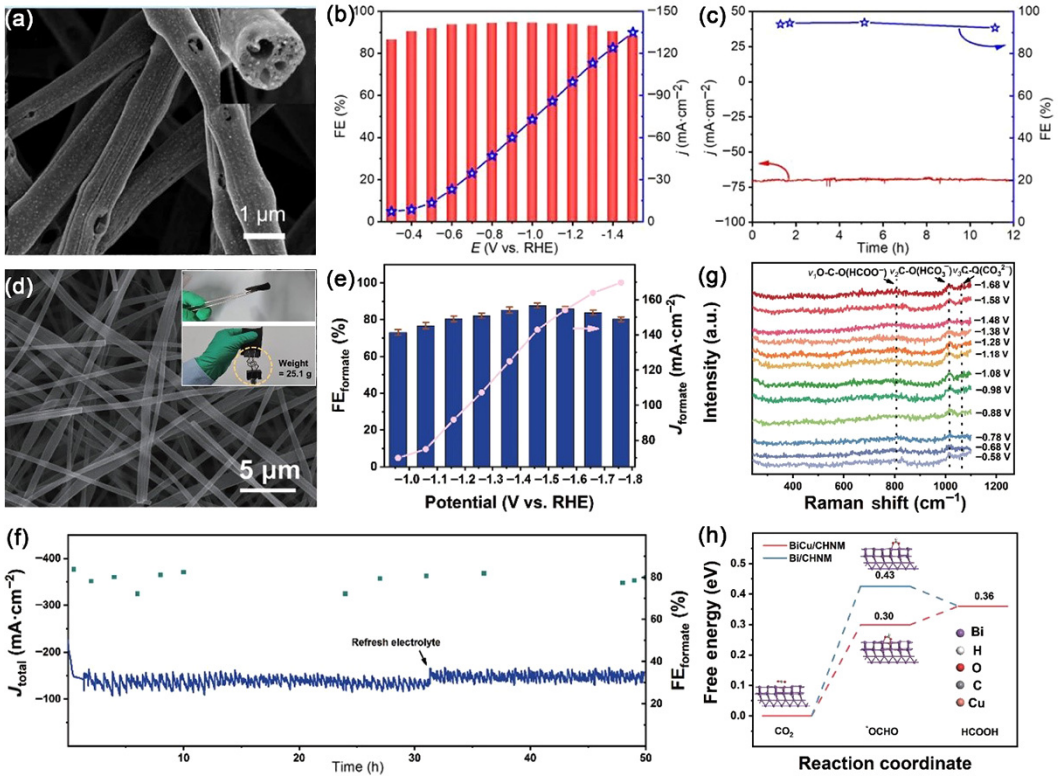

Figure 9 (a) High-magnification SEM image of the Bi@PCNF-500. (b) FE of formate and partial current density of the Bi@PCNF-500 catalyst in 1 M KOH. (c) Stability test of the Bi@PCNF-500 catalyst. Reproduced with permission from Ref. [136], © Youke Publishing Co., Ltd. 2024. (d) SEM image of the BiCu/CHNM. (e) Potential-dependent FE and partial current densities toward formate on BiCu/CHNM in the flow cell. (f) Durability test of the BiCu/CHNM in 1 M KOH electrolyte. (g) *In situ* Raman spectra of the BiCu/CHNM in CO_2-saturated 0.5 M $KHCO_3$ at different applied potentials. (h) Free energy diagram of different pathways for ECO_2RR to formate. Reproduced with permission from Ref. [137], © Science China Press 2024.

effectively leverages their respective advantages, achieving efficient ECO_2RR.

Electrospun CNFs can be directly utilized as self-supported gas diffusion electrodes (GDEs) in flow battery configurations. Song et al. synthesized a self-supported BiCu/carbon hybrid nanofiber membrane (BiCu/CHNM) using an electrospinning-calcination approach and employed it directly as the working electrode in a flow cell (Fig. 9(d)) [137]. At a biased current density of 142.9 mA·cm^{-2} for CO_2RR, the Faradaic efficiency reached as high as 87.67% (Fig. 9(e)). During stability tests, the FE_{HCOOH} of BiCu/CHNM electrodes remained above 80% at a local current density of > 100 mA·cm^{-2}, sustaining for 50 h (Fig. 9(f)). The enhanced conductivity of carbon nanofiber networks lowers the reduction of energy barriers for $HCOO^-$ formation on Bi (012) planes due to copper doping, as confirmed by *in situ* Raman spectroscopy and density functional theory calculations (Figs. 9(g) and 9(h)).

5.2.2 CO

CO possesses a broad spectrum of application prospects, encompassing the chemical and metallurgical industries. Fischer–Tropsch (FT) chemistry can convert CO into long-chain hydrocarbons under certain conditions. These hydrocarbons serve as crucial feedstocks for the production of a multitude of chemical products and intermediates. Previous studies have shown that bimetallic and heterostructure catalysts are promising catalysts for CO production [138, 139].

Bimetallic catalysts offer an advantage in ECO_2RR by fine-tuning the electronic structure of each metal constituent, which in turn modulates the binding energy of reaction intermediates. This merit not only optimizes the interaction between the catalyst and key reaction species but also mitigates the competing HER. In 2021, Hao and his colleagues reported the concept of atomic-polymer hybridization [140]. Preparing homogeneous solid solution alloy nanoparticles of AuNi with positively charged Ni centers on CNFs through electrospinning and graphitization processes (Fig. 10(a)). The Au_1Ni_1/CNFs catalyst, graphitized at 1000 °C, exhibited a FE_{CO} value of 92% at −0.98 V vs. RHE (Fig. 10(b)), which is significantly higher than pure Au and Ni nanoparticles. Subsequent DFT calculations indicated that the combination of Ni with Au increases the positive charge of the d-band center, reducing the free energy barrier for the activation of CO_2 into *COOH and the desorption of *CO (Fig. 10(c)). In 2022, Hao's group reported a strain relaxation strategy to determine the lattice strain of bimetallic alloys (Fig. 10(d)) [141]. CNFs-supported strained PdNi alloy nanoparticles were prepared using the electrospinning method. By thermally driven strain relaxation, the lattice strain of the metal alloy was controllable and optimized. Results showed that the strained PdNi alloys (s-PdNi) with a strain of 2.3% exhibited the best FE_{CO} of 96.6% at −0.88 V vs. RHE (Fig. 10(e)). DFT calculations revealed that strain relaxation effectively improved the activity and selectivity of ECO_2RR by optimizing the formation energies of *COOH and *CO intermediates on the s-PdNi alloy surface (Fig. 10(f)).

In the process of ECO_2RR, PCET is a crucial step, and the slow kinetics of this process is a major challenge in improving catalytic efficiency. Heterostructure engineering is an effective strategy to

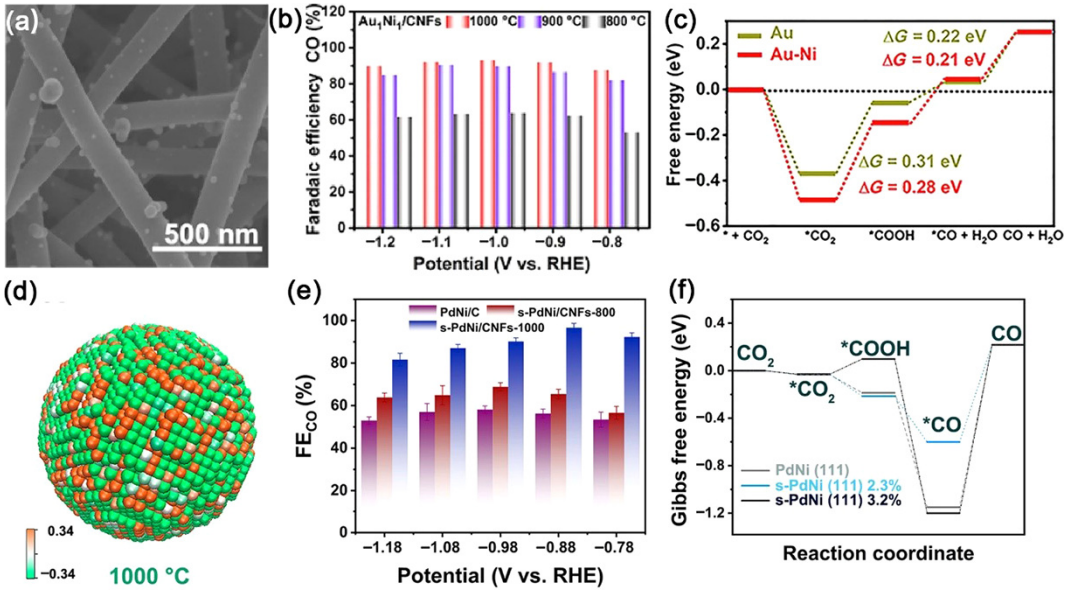

Figure 10 (a) SEM image of the Au_1Ni_1/CNFs. (b) FE_{CO} of the Au_1Ni_1/CNFs prepared at 800, 900, and 1000 °C. (c) DFT calculations of the free energy diagrams for ECO_2RR pathways on AuNi (111) catalyst surface. Reproduced with permission from Ref. [140], © Elsevier B.V. 2020. (d) Surface strains of s-PdNi nanoparticles prepared at 1000 °C, calculated by molecular dynamics simulations. (e) FE_{CO} of the s-PdNi. (f) Calculated free energy diagrams for ECO_2RR to CO on s-PdNi. Reproduced with permission from Ref. [141], © American Chemical Society 2022.

facilitate charge conduction and optimize the PCET process. Wei et al. fabricated a $Ni/Ni_3ZnC_{0.7}$ heterostructure catalyst supported on porous N-doped carbon nanofibers (PNFC) through electrospinning [142]. The nickel acetate, zinc acetate, and zinc oxide precursors were dispersed in polyacrylonitrile nanofibers and then annealed at 900 °C under an Ar atmosphere. During the pyrolysis process, the formation of PNFC occurred as the zinc-containing components evaporated. Concurrently, the $Ni/Ni_3ZnC_{0.7}$ heterostructure nanoparticles formed and were homogeneously embedded within the carbon nanofibers. As a CO_2RR electrocatalyst, the $Ni/Ni_3ZnC_{0.7}$ in 0.5 M $KHCO_3$ exhibited a high FE_{CO} of 91.5% at −0.8 V and a partial current density of 11 $mA{\cdot}cm^{-2}$, demonstrating excellent long-term stability over 45 h of continuous electrolysis. The authors attribute the superior performance of the $Ni/Ni_3ZnC_{0.7}$ to the enhanced charge transfer process at the interface.

In the process of ECO_2RR, PCET is a crucial step, and the slow kinetics of this process is a major challenge in improving catalytic efficiency. Heterostructure engineering is an effective strategy to facilitate charge conduction and optimize the PCET process. Wei et al. fabricated a $Ni/Ni_3ZnC_{0.7}$ heterostructure catalyst supported on PNFC through electrospinning [142]. The nickel acetate, zinc acetate, and zinc oxide precursors were dispersed in polyacrylonitrile nanofibers and then annealed at 900 °C under an Ar atmosphere. During the pyrolysis process, the formation of PNFC occurred as the zinc-containing components evaporated. Concurrently, the $Ni/Ni_3ZnC_{0.7}$ heterostructure nanoparticles formed and were homogeneously embedded within the carbon nanofibers. As a CO_2RR electrocatalyst, the $Ni/Ni_3ZnC_{0.7}$ in 0.5 M $KHCO_3$ exhibited a high FE_{CO} of 91.5% at −0.8 V and a partial current density of 11 $mA{\cdot}cm^{-2}$, demonstrating excellent long-term stability over 45 h of continuous electrolysis. The authors attribute the superior performance of the $Ni/Ni_3ZnC_{0.7}$ to the enhanced charge transfer process at the interface.

5.2.3 *Others (CH_4 and C_2H_4)*

In the products generated through the ECO_2RR, CH_4 is recognized as a pivotal feedstock for the synthesis of various chemical compounds, particularly aromatic hydrocarbons [143, 144]. Consequently, the development of ECO_2RR, which enables the selective transformation of CO_2 into CH_4, is of significant importance in the fields of chemical engineering and sustainable energy practices [145]. A Ru-CNF catalyst was prepared via electrospinning techniques to reduce CO_2 to CH_4 in H_2/CO_2 fuel cells [146]. The catalyst exhibited a CH_4 production rate of 308.46 $\mu mol{\cdot}g_{cat}^{-1}{\cdot}h^{-1}$ at 170 °C. The authors attribute the enhanced ECO_2RR performance of the Ru-CNF to the uniform dispersion of Ru nanoparticles within the CNF matrix and the synergistic effect between Ru sites and nitrogen species, which results in an increased number of active sites for CO_2 reduction, thereby boosting the catalytic activity. A La_2CuO_4 nanobamboo (La_2CuO_4 NBs) perovskite catalyst with rich twin boundaries was prepared by Huang et al. [147]. When used as a catalyst for ECO_2RR, La_2CuO4 NBs show a high FE toward C_2H_4 of 60% at −1.0 V vs. RHE. The total geometric current density of the La_2CuO_4 NBs remains stable for up to 12 h during the stability test, and only subtle fluctuation was observed. This is mainly due to the strong adsorption affinity of La_2CuO_4 NBs for CO intermediates, which improves the selectivity toward C_2 products.

In conclusion, combining of CNFs with metallic species markedly enhances the reactivity of the ECO_2RR. These catalysts leverage unique structural features to increase active site exposure and finely tune their electronic structure. Such fine-tuning improves the selectivity towards particular products.

5.3 Metal nanofibers as the ECO_2RR catalyst

ECO_2RR can convert CO_2 into molecules such as CO, HCOOH, and CH_3OH using electricity generated from renewable energy sources, realizing recycling, and thereby reducing dependence on fossil fuels. Metal nanofibers have a high specific surface area, good

electrical conductivity, and unique electronic structure, providing potential advantages for ECO_2RR. Early synthesis methods are relatively simple but have some limitations. For example, metal nanofibers prepared by some physical methods have uneven sizes. The electrospinning method produced nanofibers from a solution containing a metal precursor by applying a high-voltage electric field. This method allows precise control over the diameter and length of nanofibers, enabling the production of metal nanofibers with high specific surface area and excellent flexibility, and is suitable for large-scale fabrication.

5.3.1 CO

Single metal oxides usually have a relatively simple structure and preparation method with low cost. They exhibit high stability and resist structural changes under reaction conditions [126]. Zhang et al. synthesized cobalt-free perovskite oxide $Sr_2Fe_{1-5}Mo_{0.5}O_{6-8}$ nanofibers (SFM-NF) with unique double perovskite structure and reticular nanofiber morphology by electrospinning technology (Figs. 11(a) and 11(b)) [148]. The larger specific surface area and oxygen vacancies increase the adsorption sites of CO_2, accelerate the adsorption, dissociation, and activation processes of CO_2, and thereby increase the reaction rate. At 800 °C and 2.0 V, the current density of the SFM-NF single cell reaches 1.173 $A{\cdot}cm^{-1}$ (Fig. 11(c)). In the stability test, SFM-NF maintained no significant performance degradation for 45 h, and the FE_{CO} exceeded 90% (Fig. 11(d)). However, the catalytic activity and selectivity of single metal oxides are often limited. They may require a higher overpotential (the additional voltage required to drive the reaction) to achieve ECO_2RR, and the selectivity for specific products is limited, which may lead to the generation of multiple by-products.

In bimetallic oxides, there is a synergistic effect between two different metal ions, which can significantly improve the catalytic performance of ECO_2RR [149]. For example, the electronic structures of the two metal ions interact with each other, changing the adsorption and activation ability of the catalyst for CO_2, thereby reducing the overpotential of the reaction. Moreover, the interaction between bimetals can also regulate the selectivity of the catalyst, making the reaction more inclined to generate specific products. Jiang et al. prepared tin-cobalt bimetallic oxide/carbon matrix composite material (SnCo-HNT) by electrospinning technology (Fig. 11(e)) [150]. In an H-type cell, the FE of SnCo-HNT for C_1 products reaches 98.1% at −0.9 V (vs. RHE), and it has the highest selectivity for CO (Fig. 11(f)). In a flow cell, it has a Faradaic efficiency of 91.2% for C_1 products at 241.3 $mA{\cdot}cm^{-2}$ (Fig. 11(g)).

Composite nanofibers have significant advantages in CO_2RR. Their high specific surface area can provide a large number of active sites, enabling the catalyst to full contact with CO_2 and improving reaction efficiency and rate. Akromjon et al. prepared a new hybrid $La_{0.6}Sr_{0.4}Co_{0.15}Fe_{0.8}Pd_{0.05}O_{3-\delta}$ nanofiber electrode (H-LSCFP) [151]. At 700 °C, the LSCFP nanofibers underwent consecutive treatment in 100% H_2 and CO_2, forming a perovskite phase containing Co metal nanocatalysts and a high concentration of surface oxygen species. This unique structure enhances effective CO_2 adsorption. The solid oxide electrolysis cells (SOECs) with the H-LSCFP electrode achieved an outstanding current density of

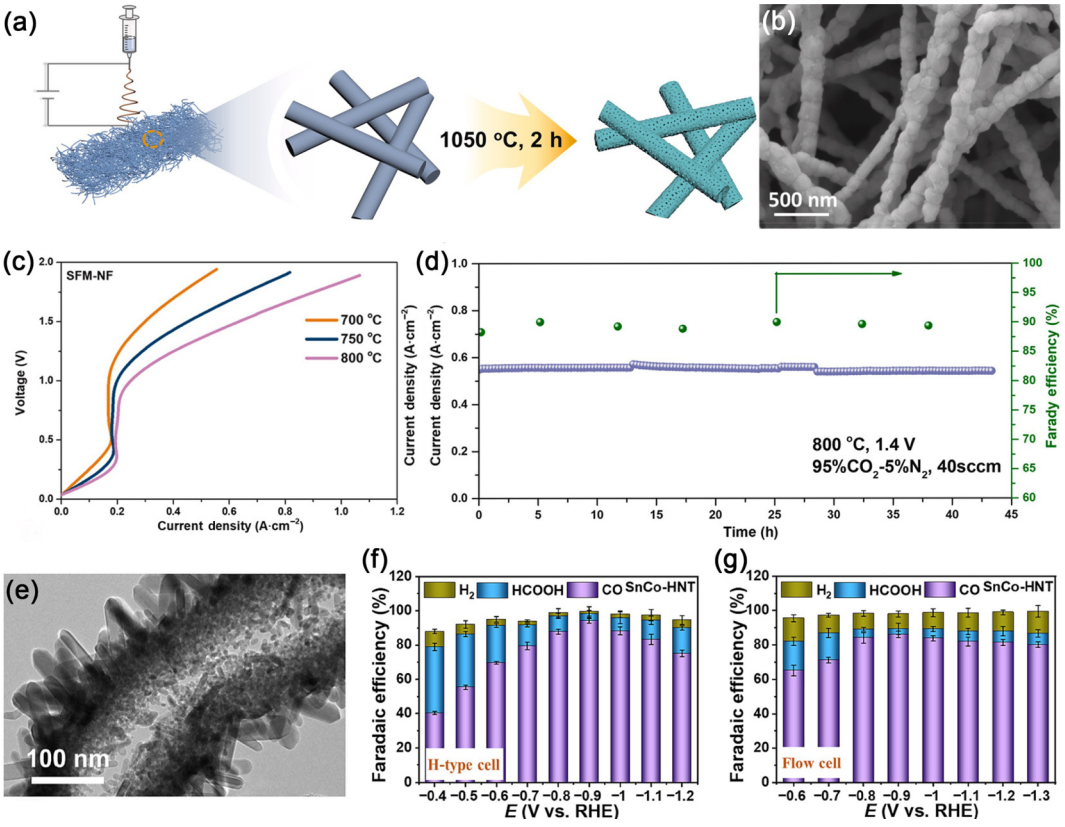

Figure 11 (a) A scheme of the preparation of the electrospun SFM-NF. (b) SEM image of the SFM-NF. (c) *i*–*V* curves of the SFM-NF catalysts. (d) Long-term stability test of SFM-NF cathode at an applied voltage of 1.4 V. Reproduced with permission from Ref. [148], © Elsevier B.V. 2023. (e) TEM image of the SnCo-HNT. (f) The FEs of SnCo-HNT at cathode potential of −0.4–−1.2 V_{RHE} in an H-type cell. (g) The FEs of the SnCo-HNT at −0.6–−1.3 V_{RHE} in a flow cell. Reproduced with permission from Ref. [150], © Science Press and Dalian Institute of Chemical Physics, Chinese Academy of Sciences 2023.

2.2 A·cm^{-2} at 800 °C and 1.5 V. Zong et al. synthesized ZnO nanoparticle catalysts rich in oxygen vacancies through electrospinning technology to achieve efficient ECO_2RR [152]. Results show that using $Zn(CH_3COO)_2$ precursor helps generate oxygen vacancies in the ZnO catalyst, thereby enhancing CO_2 adsorption and stabilizing intermediates. In a flow cell configuration, the ZnO nanoparticle catalyst (p-ZnO-800) can obtain a current density of 150 mA·cm^{-2} with a FE_{CO} of > 80%, which is of great significance for the industry.

5.3.2 HCOOH

By controlling the pyrolysis temperature and time, the structure and properties of metal nanofibers can be adjusted [153]. Electrospinning combined with pyrolysis treatment can prepare metal nanofibers with special structures and properties. Li et al. prepared an In-Bi bimetallic nanofiber catalyst with a controllable crystal plane by electrospinning and electrochemical reduction methods (Fig. 12(a)) [154]. The synthesized In-Bi bimetallic nanofibers (Bi_5In_5 NFs) have a high proportion of InBi (200) crystal plane which has a high activity and selectivity for formate. At the same time, the synergistic effect of bimetals stabilizes reaction intermediates and inhibits the hydrogen evolution reaction. The maximum Faradaic efficiency of Bi_5In_5 NFs for formate is 96.8% at −1.1 V vs. RHE (Fig. 12(b)).

In electrospinning, calcination is usually used to remove organic substances in nanofibers, improve the crystallinity of nanofibers, and enhance the thermal stability of nanofibers. By controlling the calcination temperature and time, the structure and properties of the nanofiber can be adjusted. Li et al. prepared SnO_2/LaOCl nanofibers with a built-in electric field by electrospinning [155]. SnO_2/LaOCl nanofibers reached a Faradaic efficiency of C_1 products close to 100% when the voltage is −0.9–−1.1 V vs. RHE in an H-cell. When the voltage is −1.2V vs. RHE, FE_{HCOOH} reaches up to 90.1% (Fig. 12(c)). SnO_2/LaOCl nanofibers show excellent performance in an H-cell and still have good stability after 10 h of electrolysis. In a flow cell, the current density of the SnO_2/LaOCl nanofibers reaches nearly 400 mA·cm^{-2} with high FE_{HCOOH} (83.4%) (Figs. 12(d) and 12(e)). DFT calculations demonstrate that SnO_2/LaOCl nanofibers exhibit a more robust adsorption capacity for CO_2, which is favorable for the CO_2 reduction reaction (Fig. 12(f)).

Electrospinning offers a versatile method for fabricating nanofibers, with various post-treatments such as pyrolysis, electrochemical reduction, calcination, and annealing capable of further tailoring the structure and properties of the nanofiber [156]. These treatments enable control over crystal structures, formation of specific interfaces or built-in electric fields, and introduction of oxygen vacancies. Such diverse preparation strategies provide valuable approaches for designing and developing efficient materials for ECO_2RR. Future research can build on these techniques to refine and optimize material synthesis processes, aiming for even higher performance.

6 Conclusions and outlook

The increasing atmospheric concentration of CO_2 puts serious environmental risks in people's lives and development. Converting CO_2 to value-added fuels and chemicals via ECO_2RR is expected to mitigate the CO_2 emission and contribute to economic growth, addressing both of environmental and energy problems. However, the key challenges for the large-scale application of ECO_2RR lie in designing efficient catalysts with high activity and selection. Electrospinning provided a safe, facile, and straight way to produce nanofibers with a high surface area-to-volume ratio, controllable dimensions, tunable functionalities, lightweight characteristics, and high porosity. Those electrospun nanofibers show characteristic advantages of exposure active sites, tunable functionality, and high selectivity as a catalyst for ECO_2RR. In this review, we first took a detailed look at the principle of electrospinning technology and summarized the key factors that influence the electrospinning process, including solution parameters (concentration, viscosity, and conductivity), environment parameters (temperature and

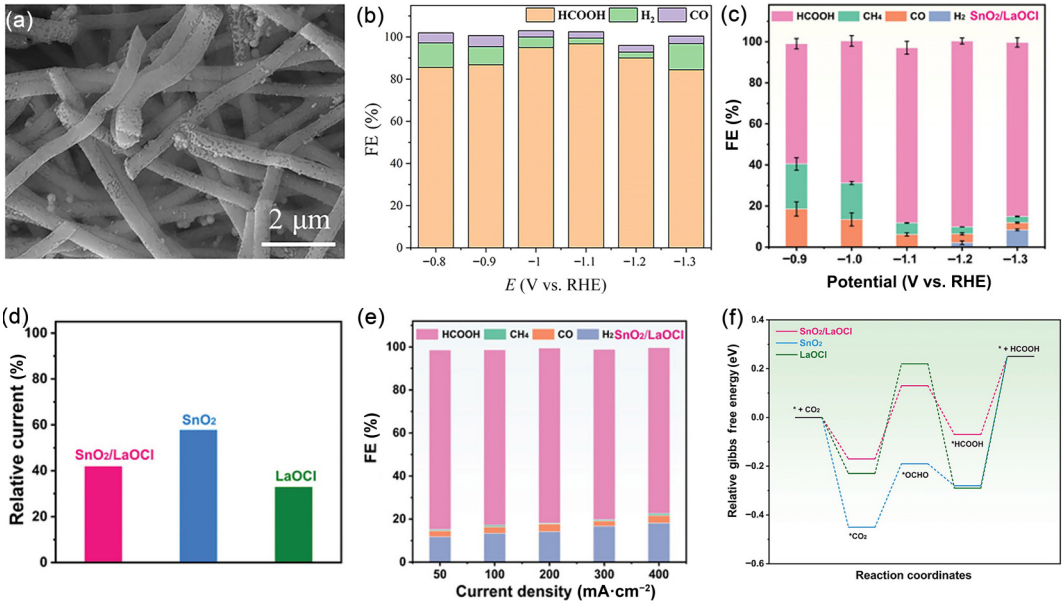

Figure 12 (a) SEM image of Bi_5In_5 NFs. (b) FE for HCOOH, H_2, and CO at different potentials on Bi_5In_5 NFs. Reproduced with permission from Ref. [154], © The Royal Society of Chemistry 2023. (c) FE of the products for SnO_2/LaOCl NFs. (d) The decreased percentages of current density after 10 h of continuous electrolysis at −1.1 V_{RHE} of SnO_2/LaOCl NFs. FEs of products for SnO_2/LaOCl NFs in the flow-cell at various current densities. (f) DFT calculations of reaction pathways for ECO_2RR on the surface of SnO_2/LaOCl NFs. Reproduced with permission from Ref. [155], © Wiley-VCH GmbH 2024.

humidity), and electrospinning parameter (applied voltage and tip-to-collector distance). With the optimized parameters, various nanofibers were produced, such as carbon nanofiber, metal nanofiber, and composite nanofiber (carbon nanofiber with metal compound). Then we discussed the emerging progress of electrospun nanomaterials as catalysts for the ECO_2RR toward different products from the perspective of materials design strategies.

Extensive research on ECO_2RR has primarily focused on developing electrocatalysts with enhanced selectivity for specific products and improved stability. Table 1 summarizes the recent performance of electrospun materials reported in the literatures. For ECO_2RR technology to advance from laboratory studies to industrial-scale applications, it is crucial to adopt a holistic approach that ensures both efficiency and durability under practical conditions. Based on previous studies [157], the following key parameters are critical for achieving industrial performance benchmarks. (1) FE: FE measures the proportion of the electrical charge utilized for the formation of the desired product relative to the total current. Low FE leads to increased by-products, complicating product separation and escalating industrial costs for purification and energy consumption. At present, only C_1 products like CO and formic acid can achieve near-unity FE (~ 100%). In contrast, multicarbon (C_{2+}) products generally exhibit lower FE. For example, CH_4, C_2H_4, and CH_3OH can reach FE values exceeding 80%, while C_2H_5OH achieves 52%, and C_3H_7OH remains limited to 30%. (2) Current density: Current density serves as a key indicator of catalytic activity, reflecting the reaction rate of an electrocatalytic process. To meet industrial requirements, catalysts must sustain high activity to achieve production rates of ECO_2RR products exceeding 200 $mA{\cdot}cm^{-2}$. (3) Stability: Stability encompasses the consistency of current density, Faradaic efficiency, and energy efficiency over time. It is influenced by factors such as catalyst deactivation, membrane degradation, electrode flooding, and operational impurities. Industrial electrocatalysts must demonstrate prolonged stability, maintaining performance over extended periods to ensure reliability. However, most CO_2RR studies to date have evaluated catalysts for less than 100 h, falling significantly short of industrial standards.

Despite the enormous progress in understanding the fundamentals of the electrospinning process and connecting the electrospinning parameters to the fiber morphologies, structures, and properties. The basic lab-scale set-up of the electrospinning machine with a low production amount is far from the practical application in view of production scale, cost, and sustainability. First of all, most of the current nanofibers are produced from commercial polymers, such as polyacrylonitrile, polyvinylpyrrolidone, and polyethylene glycol, due to their high electrospinnability. Since the electrospinnable solution system is the footstone for the electrospinning process, it is critical to expand the range of electrospinning-friendly materials to develop electrospinning as a broadly applied processing technology. Meanwhile, large amounts of solvents are involved in industrial upscale, resulting in both economic and environmental concerns. Therefore, it is critical to develop methods based on "green" solvents or even solvent-free systems. In the case of large-scale production, the current single-needle system with a low pumping rate results in a low yield that is far from the industrial requirement. Therefore, different electrospinning designs (muti-needle systems) and accessories are needed to increase the production scale and meet the demand of the market. However, ensuring the stability of electrostatic spinning, fiber homogeneity, and continuity is very important for the mass production of fibers. Addressing these critical challenges is essential for designing highly efficient nanofiber catalysts for industrial-scale CO_2 electrolysis.

Despite significant advancements in the development of electrospun nanofibers as catalysts for ECO_2RR, product selectivity remains limited, with CO and HCOOH being the predominant products. This limited range of products reflects challenges in controlling reaction pathways and achieving higher-value multicarbon products, which are essential for enhancing the

Table 1 ECO_2RR performance of various electrospun nanofibers reported in the literatures

Type of nanofibers	Catalyst	Electrolyte	Potential (V vs. RHE)	Main product	FE (%)	Electrolyzer	References
Carbon nanofibers	$K_{0.66}$Ni-NC	0.1 M $KHCO_3$	−0.8–−1.6	CO	> 90.0	H-cell	[119]
	SnN-HF-5	0.5 M $KHCO_3$	−0.47	CO	98.0	H-cell	[120]
	Ni-PCNF	0.1 M $KHCO_3$	−1.50	CO	98.6	H-cell	[121]
	Fe-N-CF	0.5 M $NaHCO_3$	−0.51	CO	97.0	H-cell	[124]
	Sn/NCNFs	1 M KOH	−0.40	CO	96.5	H-cell	[125]
Composite nanofibers	SnO_2 HNTs	0.5 M $NaHCO_3$	−1.10	HCOOH	75.0	H-cell	[134]
	GaN/In_2O_3@PCNF	0.5 M $KHCO_3$	−0.90	HCOOH	87.0	H-cell	[135]
	Bi@PCNF-500	1.0 M KOH	−1.10	HCOOH	94.9	Flow-cell	[136]
	BiCu/CHNM	0.1 M $KHCO_3$	−1.46	HCOOH	87.7	Flow-cell	[137]
	Au_1Ni_1/CNFs	0.1 M $KHCO_3$	−0.98	CO	92.0	H-cell	[140]
	s-PdNi	0.1 M $KHCO_3$	−0.88	CO	96.6	H-cell	[141]
	Ni/$Ni_3ZnC_{0.7}$	0.5 M $KHCO_3$	−0.80	CO	91.5	H-cell	[142]
	La_2CuO_4 NBs	0.1M $KHCO_3$	−1.00	C_2H_4	60.0	H-cell	[147]
Metal nanofibers	SnCo-HNT	0.1 M $KHCO_3$	−0.90	CO	91.2	H-cell	[150]
	p-ZnO-800	0.1 M $KHCO_3$	−1.00	CO	82.9	Flow cell	[152]
	Bi_5In_5 NFs	1.0 M KOH	−1.10	HCOOH	96.8	Flow cell	[154]
	SnO_2/LaOCl NFs	1.0 M KOH	−2.31	HCOOH	—	Flow cell	[155]

economic viability of ECO_2RR. During the ECO_2RR process, carbon-based materials often become increasingly hydrophilic, which undesirably promotes the hydrogen evolution reaction over CO_2 reduction, thereby diminishing the selectivity for ECO_2RR products. The wettability of electrodes plays a critical role in the adsorption and transport of reactants and products at the solid–liquid–gas triple-phase interface. A super hydrophilic electrode surface can lead to flooding and the obstruction of gas transport pores, potentially contributing to the narrow potential range for formate selectivity. To address this issue, surface coating strategies can enhance the stability of CNF-based catalysts during prolonged cycling. Another major challenge lies in the insufficient stability of catalysts under prolonged operational conditions and the low current densities, both of which hinder the scalability and industrial applicability of ECO_2RR technology.

To overcome these challenges, future development of electrospun nanomaterials for ECO_2RR will focus on the following areas:

(1) Electrospun nanofibers functionalized with active sites can effectively modulate their electronic structure, influencing the reaction pathways. The integration of the active site and single-atom catalyst modification and structural regulation synergistically enhances catalytic activity and selectivity. These findings provide valuable theoretical insights and practical guidance for advancing the design of efficient ECO_2RR catalysts. Future research should focus on exploring the synergistic effects of various structural regulation strategies, such as element doping [158], vacancies [159], and synergistic effect of cationic and aprotic solvents [160], and assessing their feasibility in real-world applications to further promote the development and implementation of ECO_2RR technology.

(2) The interactions between reactants, active sites, and catalyst components during ECO_2RR remain unclear, posing a critical challenge for further catalyst research. Advanced techniques, such as *in situ* Fourier transform infrared spectroscopy and *in situ* X-ray absorption fine structure, are needed to analyze the formation rates of intermediate products during catalysis and to clarify the molecular, atomic, and electronic structural relationships under real-time reaction conditions.

(3) The integration of machine learning and mathematical modeling can significantly reduce the time and effort required for experimental work. Theoretical computations have demonstrated unique advantages in catalyst screening, and it is anticipated that data-driven high-throughput methods will play a dominant role in the future of intelligent nanofiber catalyst synthesis.

Data availability

All data needed to support the conclusions in the paper are presented in the manuscript. Additional data related to this paper may be requested from the corresponding author upon request.

Acknowledgements

This work was financially supported by the National Natural Science Foundation of China (Nos. 22475003, 22479001, 22405161, and 22209063), the Natural Science Foundation of Hubei Province (No. 2022CFB820), and the Science Fund for Distinguished Young Scholars of Anhui Province (No. 2308085J16).

Declaration of competing interest

All the contributing authors report no conflict of interests in this work.

Author contribution statement

Y. B. L.: Writing – original draft. P. F.: Conceptualization, writing – original draft. Z. Z. W.: Writing – original draft. Y. Y.: Writing – review & editing. Y. Z. (Yong Zheng): Writing – original draft. Y. Z. (Yu Zhang): Writing – review & editing. M. K. L.: Conceptualization, writing – review & editing. All the authors have approved the final manuscript.

Use of AI statement

None.

References

[1] Chu, S.; Majumdar, A. Opportunities and challenges for a sustainable energy future. *Nature* **2012**, *488*, 294–303.

[2] Xia, R.; Overa, S.; Jiao, F. Emerging electrochemical processes to decarbonize the chemical industry. *JACS Au* **2022**, *2*, 1054–1070.

[3] Wang, L. M.; Chen, W. L.; Zhang, D. D.; Du, Y. P.; Amal, R.; Qiao, S. Z.; Wu, J. B.; Yin, Z. Y. Surface strategies for catalytic CO_2 reduction: From two-dimensional materials to nanoclusters to single atoms. *Chem. Soc. Rev.* **2019**, *48*, 5310–5349.

[4] Chen, S. H.; Ye, C. L.; Wang, Z. W.; Li, P.; Jiang, W. J.; Zhuang, Z. C.; Zhu, J. X.; Zheng, X. B.; Zaman, S.; Ou, H. H. et al. Selective CO_2 reduction to ethylene mediated by adaptive small-molecule engineering of copper-based electrocatalysts. *Angew. Chem., Int. Ed.* **2023**, *135*, e202315621.

[5] Chen, S. H.; Zheng, X. B.; Zhu, P.; Li, Y. P.; Zhuang, Z. C.; Wu, H. J.; Zhu, J. X.; Xiao, C. H.; Chen, M. Z.; Wang, P. S. et al. Copper atom pairs stabilize *OCCO dipole toward highly selective CO_2 electroreduction to C_2H_4. *Angew. Chem., Int. Ed.*, in press, https://doi.org/10.1002/anie.202411591.

[6] Newman, R.; Noy, I. The global costs of extreme weather that are attributable to climate change. *Nat. Commun.* **2023**, *14*, 6103.

[7] Zeng, M.; Fang, W. S.; Cen, Y. R.; Zhang, X. Y.; Hu, Y. M.; Xia, B. Y. Reaction environment regulation for electrocatalytic CO_2 reduction in acids. *Angew. Chem., Int. Ed.* **2024**, *63*, e202404574.

[8] Chen, Y. J.; Jiang, B.; Hao, H. G.; Li, H. J.; Qiu, C. Y.; Liang, X.; Qu, Q. Y.; Zhang, Z. D.; Gao, R.; Duan, D. M. et al. Atomic-level regulation of cobalt single-atom nanozymes: Engineering high-efficiency catalase mimics. *Angew. Chem.* **2023**, *135*, e202301879.

[9] Mu, X. Q.; Liu, S. L.; Zhang, M. Y.; Zhuang, Z. C.; Chen, D.; Liao, Y. R.; Zhao, H. Y.; Mu, S. C.; Wang, D. S.; Dai, Z. H. Symmetry-broken Ru nanoparticles with parasitic Ru-Co dual-single atoms overcome the volmer step of alkaline hydrogen oxidation. *Angew. Chem.* **2024**, *136*, e202319618.

[10] Guan, S. Y.; Yuan, Z. L.; Zhao, S. Q.; Zhuang, Z. C.; Zhang, H. H.; Shen, R. F.; Fan, Y. P.; Li, B. J.; Wang, D. S.; Liu, B. Z. Efficient hydrogen generation from ammonia borane hydrolysis on a tandem ruthenium-platinum-titanium catalyst. *Angew. Chem., Int. Ed.* **2024**, *63*, e202408193.

[11] Zhang, Z.; Huang, X.; Chen, Z.; Zhu, J. J.; Endrődi, B.; Janáky, C.; Deng, D. H. Membrane electrode assembly for electrocatalytic CO_2 reduction: Principle and application. *Angew. Chem., Int. Ed.* **2023**, *62*, e202302789.

[12] Guan, S. Y.; Yuan, Z. L.; Zhuang, Z. C.; Zhang, H. H.; Wen, H.; Fan, Y. P.; Li, B. J.; Wang, D. S.; Liu, B. Z. Why do single-atom alloys catalysts outperform both single-atom catalysts and nanocatalysts on MXene. *Angew. Chem., Int. Ed.* **2024**, *63*, e202316550.

[13] Han, A. L.; Sun, W. M.; Wan, X.; Cai, D. D.; Wang, X. J.; Li, F.; Shui, J. L.; Wang, D. S. Construction of Co_4 atomic clusters to enable Fe-N_4 motifs with highly active and durable oxygen reduction performance. *Angew. Chem., Int. Ed.* **2023**, *62*, e202303185.

[14] Chu, S.; Cui, Y.; Liu, N. The path towards sustainable energy. *Nat. Mater.* **2017**, *16*, 16–22.

[15] Yan, Y.; Wen, B. H.; Liu, M. K.; Lei, H.; Yang, J. F.; He, S. Y.; Qu, Z. H.; Xia, W.; Li, H. L.; Zeng, J. Orienting electron fillings in d orbitals of cobalt single atoms for effective zinc-air battery at a subzero temperature. *Adv. Funct. Mater.* **2024**, *34*, 2316100.

[16] Hu, Y. M.; Chao, T. T.; Li, Y. P.; Liu, P. G.; Zhao, T. H.; Yu, G.; Chen, C.; Liang, X.; Jin, H. L.; Niu, S. W. et al. Cooperative Ni(Co)-Ru-P sites activate dehydrogenation for hydrazine oxidation assisting self-powered H_2 production. *Angew. Chem., Int. Ed.* **2023**, *135*, e202308800.

[17] Li, L.; Li, X. D.; Sun, Y. F.; Xie, Y. Rational design of electrocatalytic carbon dioxide reduction for a zero-carbon network. *Chem. Soc. Rev.* **2022**, *51*, 1234–1252.

[18] Li, Y. P.; Niu, S. W.; Liu, P. G.; Pan, R. R.; Zhang, H. K.; Ahmad, N.; Shi, L.; Liang, X.; Cheng, M. Y.; Chen, S. H. et al. Ruthenium nanoclusters and single atoms on α-MoC/N-doped carbon achieves low-input/input-free hydrogen evolution via decoupled/coupled hydrazine oxidation. *Angew. Chem., Int. Ed.* **2024**, *63*, e202316755.

[19] Liu, Y. L.; Zhuang, Z. C.; Liu, Y. X.; Liu, N. Y.; Li, Y. X.; Cheng, Y. Y.; Yu, J. W.; Yu, R. H.; Wang, D. S.; Li, H. T. Shear-strained Pd single-atom electrocatalysts for nitrate reduction to ammonia. *Angew. Chem., Int. Ed.* **2024**, *63*, e202411396.

[20] Lv, L. Y.; Tan, H.; Kong, Y.; Tang, B.; Ji, Q. Q.; Liu, Y. Y.; Wang, C.; Zhuang, Z. C.; Wang, H. J.; Ge, M. et al. Breaking the scaling relationship in C–N coupling via the doping effects for efficient urea electrosynthesis. *Angew. Chem., Int. Ed.* **2024**, *136*, e202401943.

[21] Liang, F.; Zhang, K. W.; Zhang, L.; Zhang, Y. J.; Lei, Y.; Sun, X. L. Recent development of electrocatalytic CO_2 reduction application to energy conversion. *Small* **2021**, *17*, 2100323.

[22] Ma, F. Y.; Zhang, P. F.; Zheng, X. B.; Chen, L.; Li, Y. R.; Zhuang, Z. C.; Fan, Y. M.; Jiang, P.; Zhao, H.; Zhang, J. W. et al. Steering the site distance of atomic Cu–Cu pairs by first-shell halogen coordination boosts CO_2-to-C_2 selectivity. *Angew. Chem., Int. Ed.* **2024**, *63*, e202412785.

[23] Li, C. B.; Ji, Y.; Wang, Y. P.; Liu, C. X.; Chen, Z. Y.; Tang, J. L.; Hong, Y. W.; Li, X.; Zheng, T. T.; Jiang, Q. et al. Applications of metal-organic frameworks and their derivatives in electrochemical CO_2 reduction. *Nano-Micro Lett.* **2023**, *15*, 113.

[24] Huo, L. P.; Lv, M. H.; Li, M. J.; Ni, X. P.; Guan, J. Y.; Liu, J.; Mei, S. X.; Yang, Y. Q.; Zhu, M. M.; Feng, Q. C. et al. Amorphous MnO_2 lamellae encapsulated covalent triazine polymer-derived multi-heteroatoms-doped carbon for ORR/OER bifunctional electrocatalysis. *Adv. Mater.* **2024**, *36*, 2312868.

[25] Dai, M. Y.; Zhang, Y.; Ni, W. P.; Zhang, S. G. A perspective on electrochemical conversion of CO_2 to multicarbon chemicals in ionic liquids-based electrolytes. *Energy Lab* **2023**, *1*, 230006.

[26] Ning, S. B.; Ou, H. H.; Li, Y. G.; Lv, C. C.; Wang, S. F.; Wang, D. S.; Ye, J. H. Co^0–$Co^{\delta+}$ interface double-site-mediated C–C coupling for the photothermal conversion of CO_2 into light olefins. *Angew. Chem., Int. Ed.* **2023**, *62*, e202302253.

[27] Chen, F. J.; Mu, X. Q.; Zhou, J. L.; Wang, S. C.; Liu, Z. Y.; Zhou, D. Y.; Liu, S. L.; Wang, D. S.; Dai, Z. H. Engineering the active sites of MOF-derived catalysts: From oxygen activation to activate metal-air batteries. *Chin. J. Chem.* **2024**, *42*, 2520–2535.

[28] Zhang, M. Y.; Zhou, D. Y.; Mu, X. Q.; Wang, D. S.; Liu, S. L.; Dai, Z. H. Regulating the critical intermediates of dual-atom catalysts for CO_2 electroreduction. *Small* **2024**, *20*, 2402050.

[29] Guo, Y. J.; Liu, Z. Y.; Zhou, D. Y.; Zhang, M. Y.; Zhang, Y.; Li, R. Z.; Liu, S. L.; Wang, D. S.; Dai, Z. H. Competition and synergistic effects of Ru-based single-atom and cluster catalysts in electrocatalytic reactions. *Sci. China Mater.* **2024**, *67*, 1706–1720.

[30] Nitopi, S.; Bertheussen, E.; Scott, S. B.; Liu, X. Y.; Engstfeld, A. K.; Horch, S.; Seger, B.; Stephens, I. E. L.; Chan, K.; Hahn, C. et al. Progress and perspectives of electrochemical CO_2 reduction on copper in aqueous electrolyte. *Chem. Rev.* **2019**, *119*, 7610–7672.

[31] Burdyny, T.; Smith, W. A. CO_2 reduction on gas-diffusion electrodes and why catalytic performance must be assessed at commercially-relevant conditions. *Energy Environ. Sci.* **2019**, *12*, 1442–1453.

[32] Gao, Y.; Ge, J. L.; Zhang, J. Q.; Cao, T.; Sun, Z. Y.; Yan, W. S.; Wang, Y.; Lin, J.; Chen, W. X.; Liu, Z. Asymmetrically coordinated main group atomic In–S_1N_3 interface sites for promoting electrochemical CO_2 reduction. *Nano Res.* **2024**, *17*, 5011–5021.

[33] Qiu, W. B.; Qin, S. M.; Li, Y. B.; Cao, N.; Cui, W. R.; Zhang, Z. D.; Zhuang, Z. C.; Wang, D. S.; Zhang, Y. Overcoming electrostatic interaction via pulsed electroreduction for boosting the electrocatalytic urea synthesis. *Angew. Chem.* **2024**, *136*, e202402684.

[34] Tang, H. T.; Zhou, H. Y.; Pan, Y. M.; Zhang, J. L.; Cui, F. H.; Li, W. H.; Wang, D. S. Single-atom manganese-catalyzed oxygen evolution drives the electrochemical oxidation of silane to silanol. *Angew. Chem., Int. Ed.* **2024**, *136*, e202315032.

[35] Tao, Y.; Guan, J. P.; Zhang, J.; Hu, S. Y.; Ma, R. Z.; Zheng, H. R.; Gong, J. X.; Zhuang, Z. C.; Liu, S. J.; Ou, H. H. et al. Ruthenium single atomic sites surrounding the support pit with exceptional photocatalytic activity. *Angew. Chem., Int. Ed.* **2024**, *63*, e202400625.

[36] Wang, X. Y.; Pan, Y. Z.; Yang, J. R.; Li, W. H.; Gan, T.; Pan, Y. M.; Tang, H. T.; Wang, D. S. Single-atom iron catalyst as an advanced redox mediator for anodic oxidation of organic electrosynthesis. *Angew. Chem., Int. Ed.* **2024**, *63*, e202404295.

[37] Li, X. T.; Liu, Q.; Wang, J. H.; Meng, D. C.; Shu, Y. J.; Lv, X. Z.; Zhao, B.; Yang, H.; Cheng, T.; Gao, Q. S. et al. Enhanced electroreduction of CO_2 to C_{2+} products on heterostructured Cu/oxide electrodes. *Chem* **2022**, *8*, 2148–2162.

[38] Wang, M.; Chen, C. J.; Jia, S. Q.; Han, S. T.; Dong, X.; Zhou, D. W.; Yao, T.; Fang, M. H.; He, M. Y.; Xia, W. et al. Enhancing C_{2+} product selectivity in CO_2 electroreduction by enriching intermediates over carbon-based nanoreactors. *Chem. Sci.* **2024**, *15*, 8451–8458.

[39] Xu, L.; Ma, X. D.; Wu, L. M.; Tan, X. X.; Song, X. N.; Zhu, Q. G.; Chen, C. J.; Qian, Q. L.; Liu, Z. M.; Sun, X. F. et al. *In situ* periodic regeneration of catalyst during CO_2 electroreduction to C_{2+} products. *Angew. Chem. , Int. Ed.* **2022**, *61*, e202210375.

[40] Wang, Y.; Wu, J.; Tang, S. H.; Yang, J. R.; Ye, C. L.; Chen, J.; Lei, Y. P.; Wang, D. S. Synergistic Fe–Se atom pairs as bifunctional oxygen electrocatalysts boost low-temperature rechargeable Zn-air battery. *Angew. Chem., Int. Ed.* **2023**, *62*, e202219191.

[41] Xia, J. K.; Xu, J. W.; Yu, B.; Liang, X.; Qiu, Z.; Li, H.; Feng, H. J.; Li, Y. F.; Cai, Y. J.; Wei, H. Y. et al. A metal-sulfur-carbon catalyst mimicking the two-component architecture of nitrogenase. *Angew. Chem.* **2024**, *136*, e202412740.

[42] Yang, J. R.; Zhu, C. X.; Li, W. H.; Zheng, X. S.; Wang, D. S. Organocatalyst supported by a single-atom support accelerates both electrodes used in the chlor-alkali industry via modification of non-covalent interactions. *Angew. Chem., Int. Ed.* **2024**, *63*, e202314382.

[43] Yang, J. R.; Zhu, C. X.; Wang, D. S. A simple organo-electrocatalysis system for the chlor-related industry. *Angew. Chem.* **2024**, *136*, e202406883.

[44] Zhang, Y. D.; Sun, Y. J.; Wang, Q. Y.; Zhuang, Z. C.; Ma, Z. T.; Liu, L. M.; Wang, G. M.; Wang, D. S.; Zheng, X. S. Synergy of photogenerated electrons and holes toward efficient photocatalytic urea synthesis from CO_2 and N_2. *Angew. Chem.* **2024**, *136*, e202405637.

[45] He, X. R.; Chen, J. W.; Xu, Y. F.; Shen, Y.; Zeng, Y. F.; Zhu, J. Y.; Xu, B. J.; Wang, C. Metal-organic layers induce *in situ* nano-structuring of Cu surface in electrocatalytic CO_2 reduction. *Nano Res.* **2023**, *16*, 4554–4561.

[46] Zhao, J.; Zhang, Y. X.; Zhuang, Z. C.; Deng, Y. T.; Gao, G.; Li, J. Y.; Meng, A. L.; Li, G. C.; Wang, L.; Li, Z. J. et al. Tailoring d-p orbital hybridization to decipher the essential effects of heteroatom substitution on redox kinetics. *Angew. Chem., Int. Ed.* **2024**, *136*, e202404968.

[47] Zhao, S.; Liu, M. J.; Qu, Z. H.; Yan, Y.; Zhang, Z. R.; Yang, J. F.; He, S. Y.; Xu, Z.; Zhu, Y. Q.; Luo, L. H. et al. Cascade synthesis of Fe-N_2-Fe dual-atom catalysts for superior oxygen catalysis. *Angew. Chem., Int. Ed.* **2024**, *63*, e202408914.

[48] Zheng, X. B.; Yang, J. R.; Li, P.; Jiang, Z. L.; Zhu, P.; Wang, Q. S.; Wu, J. B.; Zhang, E. H.; Sun, W. P.; Dou, S. X. et al. Dual-atom support boosts nickel-catalyzed urea electrooxidation. *Angew. Chem., Int. Ed.* **2023**, *135*, e202217449.

[49] Li, Y.; Shi, G. Q.; Chen, T.; Zhu, L.; Yu, D. F.; Sun, Y.; Besenbacher, F.; Yu, M. Simultaneous increase of conductivity, active sites and structural strain by nitrogen injection for high-yield CO_2 electro-hydrogenation to liquid fuel. *Appl. Catal. B: Environ.* **2022**, *305*, 121080.

[50] Tang, M. H.; Shen, J.; Zhang, F. T.; Zhao, Y. F.; Gan, T.; Zeng, W.; Li, R. X.; Wang, D. S.; Han, B. X.; Liu, Z. M. Upcycling of polyamide wastes to tertiary amines using Mo single atoms and Rh nanoparticles. *Angew. Chem., Int. Ed.*, in press, https://doi.org/10.1002/anie.202416436.

[51] Zhu, C. X.; Yang, J. R.; Zhang, J. W.; Wang, X. Q.; Gao, Y.; Wang, D. S.; Pan, H. G. Single-atom materials: The application in energy conversion. *Interdiscip. Mater.* **2024**, *3*, 74–86.

[52] Qiao, J. L.; Liu, Y. Y.; Hong, F.; Zhang, J. J. A review of catalysts for the electroreduction of carbon dioxide to produce low-carbon fuels. *Chem. Soc. Rev.* **2014**, *43*, 631–675.

[53] Liu, P. C.; Liu, Y. Y.; Wang, K. L.; Shi, S.; Jin, M. M.; Liu, J. X.; Qin, T.; Liu, Q.; Liu, X. J.; He, J. Revealing the role of electrode potential micro-environments in single Mn atoms for carbon dioxide and oxygen electrolysis. *Nano Res.* **2024**, *17*, 7957–7966.

[54] Zhuang, J. H.; Wang, D. S. Recent advances of single-atom alloy catalyst: Properties, synthetic methods and electrocatalytic applications. *Mater. Today Catal.* **2023**, *2*, 100009.

[55] Gan, T.; Wang, D. S. Atomically dispersed materials: Ideal catalysts in atomic era. *Nano Res.* **2024**, *17*, 18–38.

[56] Wang, L. G.; Wu, J. B.; Wang, S. W.; Liu, H.; Wang, Y.; Wang, D. S. The reformation of catalyst: From a trial-and-error synthesis to rational design. *Nano Res.* **2024**, *17*, 3261–3301.

[57] Wang, Y.; Ma, F. Y.; Zhang, G. Q.; Zhang, J. W.; Zhao, H.; Dong, Y. M.; Wang, D. S. Precise synthesis of dual atom sites for electrocatalysis. *Nano Res.* **2024**, *17*, 9397–9427.

[58] Li, Z. M.; Yan, Y.; Liu, M. J.; Qu, Z. H.; Yue, Y. C.; Mao, T.; Zhao, S.; Liu, M. K.; Lin, Z. Q. Robust ring-opening reaction via asymmetrically coordinated Fe single atoms scaffolded by spoke-like mesoporous carbon nanospheres. *Proc. Natl. Acad. Sci. USA* **2023**, *120*, e2218261120.

[59] Liu, F.; Hu, Y.; Qu, Z. H.; Ma, X.; Li, Z. F.; Zhu, R.; Yan, Y.; Wen, B. H.; Ma, Q. W.; Liu, M. J. et al. Rapid production of kilogram-scale graphene nanoribbons with tunable interlayer spacing for an array of renewable energy. *Proc. Natl. Acad. Sci. USA* **2023**, *120*, e2303262120.

[60] Yan, Y.; Liang, S.; Wang, X.; Zhang, M. Y.; Hao, S. M.; Cui, X.; Li, Z. W.; Lin, Z. Q. Robust wrinkled MoS_2/N-C bifunctional electrocatalysts interfaced with single Fe atoms for wearable zinc-air batteries. *Proc. Natl. Acad. Sci. USA* **2021**, *118*, e2110036118.

[61] Wang, C. L.; Lv, Z. H.; Yang, W. X.; Feng, X.; Wang, B. A rational design of functional porous frameworks for electrocatalytic CO_2 reduction reaction. *Chem. Soc. Rev.* **2023**, *52*, 1382–1427.

[62] Mukherjee, A.; Abdinejad, M.; Mahapatra, S. S.; Ruidas, B. C. Metal sulfide-based nanomaterials for electrochemical CO_2 reduction. *J. Mater. Chem. A* **2023**, *11*, 9300–9332.

[63] Zhou, Y.; Wang, K.; Zheng, S. J.; Cheng, X.; He, Y. X.; Qin, W.; Zhang, X. H.; Chang, H. X.; Zhong, N. B.; He, X. F. Advancements in electrochemical CO_2 reduction reaction: A review on CO_2 mass transport enhancement strategies. *Chem. Eng. J.* **2024**, *486*, 150169.

[64] Lai, W. C.; Qiao, Y.; Wang, Y. N.; Huang, H. W. Stability issues in electrochemical CO_2 reduction: Recent advances in fundamental understanding and design strategies. *Adv. Mater.* **2023**, *35*, 2306288.

[65] Wang, H. R.; Sun, R. B.; Liu, P. G.; Hu, H. H.; Ling, C.; Han, X.; Shi, Y.; Zheng, X. S.; Wu, G.; Hong, X. Interstitial carbon induces enriched $Cu^{\delta+}$ sites in Cu_2O nanoparticles to facilitate CO_2 electroreduction to C_{2+} products. *Nano Res.* **2024**, *17*, 7013–7019.

[66] Wang, P.; Wang, Q. J.; Wu, D. X.; Zhang, Y. Y.; Kang, S. X.; Wang, X. C.; Gu, J. Y.; Wu, H.; Xu, Z. H.; Jiang, Q. Enhancing osteogenic bioactivities of coaxial electrospinning nano-scaffolds through incorporating iron oxide nanoparticles and icaritin for bone regeneration. *Nano Res.* **2024**, *17*, 6430–6442.

[67] Tong, X.; Zhang, P.; Chen, P.; He, Z. S.; Kang, X. C.; Yin, Y. Y.; Cheng, Y. Y.; Zhou, M.; Jing, L. H.; Wang, C. et al. Switching CO_2 electroreduction pathways between ethylene and ethanol via tuning microenvironment of the coating on copper nanofibers. *Angew. Chem., Int. Ed.*, in press, https://doi.org/10.1002/anie.202413005.

[68] Bae, D.; Lee, T.; Kwon, W.; Oh, S. H.; Nam, D. H. Porous Cu/C nanofibers promote electrochemical CO_2-to-ethylene conversion via high CO_2 availability. *J. Mater. Chem. A* **2024**, *12*, 17295–17305.

[69] Wu, X.; Tong, Z.; Liu, Y. L.; Li, Y. X.; Cheng, Y. Y.; Yu, J. W.; Cao, P.; Zhuang, C. Q.; Shi, Q. Z.; Liu, N. Y. et al. Modification of the CuO electronic structure for enhanced selective electrochemical CO_2 reduction to ethylene. *Nano Res.* **2024**, *17*, 7194–7202.

[70] Chen, L.; Mei, S. Q.; Fu, K.; Zhou, J. Spinning the future: The convergence of nanofiber technologies and yarn fabrication. *ACS Nano* **2024**, *18*, 15358–15386.

[71] Lu, T. D.; Wang, Q.; Gu, S. S.; Sun, S. P. Beyond symmetry: Exploring asymmetric electrospun nanofiber membranes for liquid separation. *Adv. Funct. Mater.* **2024**, *34*, 2310218.

[72] Salah, B.; Abdelgawad, A.; El-Demellawi, J. K.; Lu, Q. Q.; Xia, Z. H.; Abdullah, A. M.; Eid, K. Scalable one-pot fabrication of carbon-nanofiber-supported noble-metal-free nanocrystals for synergetic-dependent green hydrogen production: Unraveling electrolyte and support effects. *ACS Appl. Mater. Interfaces* **2024**, *16*, 18768–18781.

[73] Bayat, F.; Hashtrodylar, Y.; Karimi, H.; Mehryab, F.; Haeri, A. A precise look at electrospinning parameters in fabricating the polymeric nanofibers: A review on synthetic and natural polymers. *J. Pharm. Investig.* **2024**, *54*, 699–750.

[74] Lin, C. X.; Feng, P.; Wang, D. Q.; Chen, X. Q.; Fang, Y. N.; Gao, Y. W.; Zheng, Y.; Yan, Y.; Liu, M. K. Safe, facile, and straightforward fabrication of poly(N-vinyl imidazole)/polyacrylonitrile nanofiber modified separator as efficient polysulfide barrier toward durable lithium-sulfur batteries. *Adv. Funct. Mater.*, in press, https://doi.org/10.1002/adfm.202411872.

[75] Feng, P.; Dong, K.; Xu, Y. L.; Zhang, X.; Jia, H. J.; Prell, H.; Tovar, M.; Manke, I.; Liu, F. Y.; Xiang, H. X. et al. Efficient and homogenous precipitation of sulfur within a 3D electrospun heterocatalytic rutile/anatase TiO_{2-x} framework in lithium-sulfur batteries. *Adv. Fiber Mater.* **2024**, *6*, 810–824.

[76] Wang, M.; Lin, L.; Zheng, Z. Y.; Jiao, Z. Y.; Hua, W.; Wang, G. W.; Ke, X. X.; Lian, Y. B.; Lyu, F. L.; Zhong, J. et al. Hydrophobized electrospun nanofibers of hierarchical porosity as the integral gas diffusion electrode for full-pH CO_2 electroreduction in membrane electrode assemblies. *Energy Environ. Sci.* **2023**, *16*, 4423–4431.

[77] Zhang, J.; Yu, M.; Tao, S. H. Advanced electrospinning nanomaterials: From spinning fabrication techniques to electrochemical applications. *Nano Res.* **2024**, *17*, 7077–7116.

[78] Zong, X.; Jin, Y. M.; Liu, C. J.; Yao, Y. L.; Zhang, J. Q.; Luo, W.; Züttel, A.; Xiong, Y. P. Electrospun nanofibers for electrochemical reduction of CO_2: A mini review. *Electrochem. Commun.* **2021**, *124*, 106968.

[79] Bose, G. M. Recherches sur la cause et sur la veritable téorie de l'électricité. *De l'Imprimerie de Jean Fred* **1745**.

[80] Rayleigh, L. On the equilibrium of liquid conducting masses charged with electricity. *London, Edinburgh, Dublin Philos. Mag. J. Sci.* **1882**, *14*, 184–186.
[81] Cooley, J. F. Apparatus for electrically dispersing fluids. U.S. 692631A, February 4, 1902.
[82] Formhals, A.; Morton, W. J. U.S. 705691A, 1902.
[83] Keirouz, A.; Wang, Z.; Reddy, V. S.; Nagy, Z. K.; Vass, P.; Buzgo, M.; Ramakrishna, S.; Radacsi, N. The history of electrospinning: Past, present, and future developments. *Adv. Mater. Technol.* **2023**, *8*, 2201723.
[84] Formhals, A. Process and apparatus for preparing artificial threads. U.S. Patent 1,975,504, October 2, 1934.
[85] Taylor, G. I. Disintegration of water drops in an electric field. *Proc. Roy. Soc. A: Math. Phys. Eng. Sci.* **1969**, *280*, 383–397.
[86] Taylor, G. I. Electrically driven jets. *Proc. Roy. Soc. A: Math. Phys. Eng. Sci.* **1969**, *313*, 453–475.
[87] Barhate, R. S.; Ramakrishna, S. Nanofibrous filtering media: Filtration problems and solutions from tiny materials. *J. Membrane Sci.* **2007**, *296*, 1–8.
[88] Doshi, J.; Reneker, D. H. Electrospinning process and applications of electrospun fibers. *J. Electrost.* **1995**, *35*, 151–160.
[89] Zong, X. H.; Kim, K.; Fang, D. F.; Ran, S. F.; Hsiao, B. S.; Chu, B. Structure and process relationship of electrospun bioabsorbable nanofiber membranes. *Polymer* **2002**, *43*, 4403–4412.
[90] Reneker, D. H.; Chun, I. Nanometre diameter fibres of polymer, produced by electrospinning. *Nanotechnology* **1996**, *7*, 216–223.
[91] Min, L. L.; Yuan, Z. H.; Zhong, L. B.; Liu, Q.; Wu, R. X.; Zheng, Y. M. Preparation of chitosan based electrospun nanofiber membrane and its adsorptive removal of arsenate from aqueous solution. *Chem. Eng. J.* **2015**, *267*, 132–141.
[92] Jiang, S. H.; Liu, F. Y.; Lerch, A.; Ionov, L.; Agarwal, S. Unusual and superfast temperature-triggered actuators. *Adv. Mater.* **2015**, *27*, 4865–4870.
[93] Li, Y.; Zhu, J. D.; Cheng, H.; Li, G. Q.; Cho, H.; Jiang, M. J.; Gao, Q.; Zhang, X. W. Developments of advanced electrospinning techniques: A critical review. *Adv. Mater. Technol.* **2021**, *6*, 2100410.
[94] Reneker, D. H.; Yarin, A. L.; Fong, H.; Koombhongse, S. Bending instability of electrically charged liquid jets of polymer solutions in electrospinning. *J. Appl. Phys.* **2000**, *87*, 4531–4547.
[95] Reneker, D. H.; Yarin, A. L. Electrospinning jets and polymer nanofibers. *Polymer* **2008**, *49*, 2387–2425.
[96] Zhang, Y. S.; Zhang, X. L.; Silva, S. R. P.; Ding, B.; Zhang, P.; Shao, G. S. Lithium-sulfur batteries meet electrospinning: Recent advances and the key parameters for high gravimetric and volume energy density. *Adv. Sci.* **2022**, *9*, 2103879.
[97] Aldossari, A. A.; Shannahan, J. H.; Podila, R.; Brown, J. M. Influence of physicochemical properties of silver nanoparticles on mast cell activation and degranulation. *Toxicol. In Vitro* **2015**, *29*, 195–203.
[98] Keirouz, A.; Chung, M.; Kwon, J.; Fortunato, G.; Radacsi, N. 2D and 3D electrospinning technologies for the fabrication of nanofibrous scaffolds for skin tissue engineering: A review. *WIREs Nanomed. Nanobiotechnol.* **2020**, *12*, e1626.
[99] Li, X. Y.; Chen, W. C.; Qian, Q. R.; Huang, H. T.; Chen, Y. M.; Wang, Z. Q.; Chen, Q. H.; Yang, J.; Li, J.; Mai, Y. W. Electrospinning-based strategies for battery materials. *Adv. Energy Mater.* **2021**, *11*, 2000845.
[100] Jung, J. W.; Lee, C. L.; Yu, S.; Kim, I. D. Electrospun nanofibers as a platform for advanced secondary batteries: A comprehensive review. *J. Mater. Chem. A* **2016**, *4*, 703–750.
[101] De Vrieze, S.; Van Camp, T.; Nelvig, A.; Hagström, B.; Westbroek, P.; De Clerck, K. The effect of temperature and humidity on electrospinning. *J. Mater. Sci.* **2009**, *44*, 1357–1362.
[102] Haider, A.; Haider, S.; Kang, I. K. A comprehensive review summarizing the effect of electrospinning parameters and potential applications of nanofibers in biomedical and biotechnology. *Arab. J. Chem.* **2018**, *11*, 1165–1188.
[103] Mailley, D.; Hébraud, A.; Schlatter, G. A review on the impact of humidity during electrospinning: From the nanofiber structure engineering to the applications. *Macromol. Mater. Eng.* **2021**, *306*, 2100115.
[104] Tripatanasuwan, S.; Zhong, Z. X.; Reneker, D. H. Effect of evaporation and solidification of the charged jet in electrospinning of poly(ethylene oxide) aqueous solution. *Polymer* **2007**, *48*, 5742–5746.
[105] Kim, G. T.; Lee, J. S.; Shin, J. H.; Ahn, Y. C.; Hwang, Y. J.; Shin, H. S.; Lee, J. K.; Sung, C. M. Investigation of pore formation for polystyrene electrospun fiber: Effect of relative humidity. *Korean J. Chem. Eng.* **2005**, *22*, 783–788.
[106] Luzio, A.; Canesi, E. V.; Bertarelli, C.; Caironi, M. Electrospun polymer fibers for electronic applications. *Materials* **2014**, *7*, 906–947.
[107] Uyar, T.; Besenbacher, F. Electrospinning of uniform polystyrene fibers: The effect of solvent conductivity. *Polymer* **2008**, *49*, 5336–5343.
[108] Wu, X. H.; Wang, L. G.; Yu, H.; Huang, Y. Effect of solvent on morphology of electrospinning ethyl cellulose fibers. *J. Appl. Polym. Sci.* **2005**, *97*, 1292–1297.
[109] Jacobs, V.; Anandjiwala, R. D.; Maaza, M. The influence of electrospinning parameters on the structural morphology and diameter of electrospun nanofibers. *J. Appl. Polym. Sci.* **2010**, *115*, 3130–3136.
[110] Ding, W.; Wei, S. Y.; Zhu, J. H.; Chen, X. L.; Rutman, D.; Guo, Z. H. Manipulated electrospun PVA nanofibers with inexpensive salts. *Macromol. Mater. Eng.* **2010**, *295*, 958–965.
[111] Lee, J. S.; Choi, K. H.; Ghim, H. D.; Kim, S. S.; Chun, D. H.; Kim, H. Y.; Lyoo, W. S. Role of molecular weight of atactic poly(vinyl alcohol) (PVA) in the structure and properties of PVA nanofabric prepared by electrospinning. *J. Appl. Polym. Sci.* **2004**, *93*, 1638–1646.
[112] Wu, C. M.; Chiou, H. G.; Lin, S. L.; Lin, J. M. Effects of electrostatic polarity and the types of electrical charging on electrospinning behavior. *J. Appl. Polym. Sci.* **2012**, *126*, E89–E97.
[113] Kuzume, A.; Kume, S. Spectrometric monitoring of CO_2 electrolysis on a molecularly modified copper surface. *Chem. Commun.* **2024**, *60*, 12662–12676.
[114] Hori, Y.; Kikuchi, K.; Murata, A.; Suzuki, S. Production of methane and ethylene in electrochemical reduction of carbon dioxide at copper electrode in aqueous hydrogencarbonate solution. *Chem. Lett.* **1986**, *15*, 897–898.
[115] Xue, D. P.; Xia, H. C.; Yan, W. F.; Zhang, J. N.; Mu, S. C. Defect engineering on carbon-based catalysts for electrocatalytic CO_2 reduction. *Nano-Micro Lett.* **2021**, *13*, 5.
[116] Fan, L.; Xia, C.; Yang, F. Q.; Wang, J.; Wang, H. T.; Lu, Y. Y. Strategies in catalysts and electrolyzer design for electrochemical CO_2 reduction toward C_{2+} products. *Sci. Adv.* **2020**, *6*, eaay3111.
[117] Chen, L. L.; Li, M. H.; Zhang, J. N. Tailoring microenvironment for efficient CO_2 electroreduction through nanoconfinement strategy. *Nano Res.* **2024**, *17*, 7880–7899.
[118] Dong, T.; Li, H. D.; Wang, Z. H.; Geng, Y. L.; Chang, R.; Tian, X. F.; Lai, J. P.; Feng, S. H.; Wang, L. Acidic electroreduction CO_2 to formic acid via interfacial modification of Bi nanoparticles at industrial-level current. *Nano Res.* **2024**, *17*, 5817–5825.
[119] Chuai, H.; Yang, H. B.; Zhang, S. Boosting electrochemical CO_2 reduction to CO by regulating the porous structure of carbon membrane. *ACS Appl. Mater. Interfaces* **2024**, *16*, 24823–24830.
[120] Cao, Z. Q.; Liu, S.; Xu, K. Y.; Mao, Y. X.; Wu, Y. J.; Mao, Q. Predictable interfacial mass transfer intensification of Sn-N doped multichannel hollow carbon nanofibers for the CO_2 electro-reduction reaction. *Sustain. Energy Fuels* **2021**, *5*, 3097–3101.
[121] Wang, H.; Chuai, H. Y.; Chen, X. Y.; Lin, J. L.; Zhang, S.; Ma, X. B.

Self-supported porous carbon nanofibers decorated with single Ni atoms for efficient CO_2 electroreduction. *ACS Appl. Mater. Interfaces* **2023**, *15*, 1376–1383.

[122] Zheng, W. Z.; Wang, Y.; Shuai, L.; Wang, X. Y.; He, F.; Lei, C. J.; Li, Z. J.; Yang, B.; Lei, L. C.; Yuan, C. et al. Highly boosted reaction kinetics in carbon dioxide electroreduction by surface-introduced electronegative dopants. *Adv. Funct. Mater.* **2021**, *31*, 2008146.

[123] Hao, J. C.; Zhu, H.; Zhuang, Z. C.; Zhao, Q.; Yu, R. H.; Hao, J. C.; Kang, Q.; Lu, S. L.; Wang, X. F.; Wu, J. S. et al. Competitive trapping of single atoms onto a metal carbide surface. *ACS Nano* **2023**, *17*, 6955–6965.

[124] Wang, X. J.; Wang, Y. J.; Cui, L. Y.; Gao, W. Q.; Li, X.; Liu, H.; Zhou, W. J.; Wang, J. G. Coordination-based synthesis of Fe single-atom anchored nitrogen-doped carbon nanofibrous membrane for CO_2 electroreduction with nearly 100% CO selectivity. *Chin. Chem. Lett.* **2024**, *35*, 110031.

[125] Hu, X. Z.; Liu, Y. N.; Cui, W. J.; Yang, X. X.; Li, J. T.; Zheng, S. X.; Yang, B.; Li, Z. J.; Sang, X. H.; Li, Y. Y. et al. Boosting industrial-level CO_2 electroreduction of N-doped carbon nanofibers with confined tin-nitrogen active sites via accelerating proton transport kinetics. *Adv. Funct. Mater.* **2023**, *33*, 2208781.

[126] Zong, X.; Zhang, J.; Zhang, J. Q.; Luo, W.; Züttel, A.; Xiong, Y. P. Synergistic Cu/CeO_2 carbon nanofiber catalysts for efficient CO_2 electroreduction. *Electrochem. Commun.* **2020**, *114*, 106716.

[127] Liu, S.; Cao, Y.; Liu, H.; Wang, H. L.; Zhang, B. S.; Zhang, Y. M.; Zhang, L. H.; Zhang, S.; Sun, J. Efficient electrochemical reduction of CO_2 promoted by the electrospun $Cu_{1.96}S$/Cu tandem catalyst. *Nanoscale* **2021**, *13*, 16986–16994.

[128] Narayanaru, S.; Anilkumar, G. M.; Ito, M.; Tamaki, T.; Yamaguchi, T. An enhanced electrochemical CO_2 reduction reaction on the SnO_x-PdO surface of SnPd nanoparticles decorated on N-doped carbon fibers. *Catal. Sci. Technol.* **2021**, *11*, 143–151.

[129] Li, Y. M.; Jin, Y. M.; Zhang, X. B.; Fu, M. Y.; Lin, R. F.; Li, G. S.; Xiong, Y. P. cAIMD simulations guided design of atomic praseodymium doping In-Bi nanofibers for high-energy-efficiency CO_2 electrolysis to formate in ultra-wide potential window. *Adv. Funct. Mater.* **2024**, *34*, 2404660.

[130] Zong, X.; Jin, Y. M.; Zhang, X. B.; Zhang, J. Q.; Li, X.; Xiong, Y. P. Stabilization of oxidation state in ZnO decorated-CeO_2 for enhanced formation of CO in CO_2 electroreduction. *Appl. Surf. Sci.* **2023**, *609*, 155235.

[131] Li, L.; Ozden, A.; Guo, S. Y.; García de Arquer, F. P.; Wang, C. H.; Zhang, M. Z.; Zhang, J.; Jiang, H. Y.; Wang, W.; Dong, H. et al. Stable, active CO_2 reduction to formate via redox-modulated stabilization of active sites. *Nat. Commun.* **2021**, *12*, 5223.

[132] Li, L.; Liu, Z. Y.; Yu, X. H.; Zhong, M. Achieving high single-pass carbon conversion efficiencies in durable CO_2 electroreduction in strong acids via electrode structure engineering. *Angew. Chem.* **2023**, *135*, e202300226.

[133] Yu, X. H.; Xu, Y. T.; Li, L.; Zhang, M. Z.; Qin, W. H.; Che, F. L.; Zhong, M. Coverage enhancement accelerates acidic CO_2 electrolysis at ampere-level current with high energy and carbon efficiencies. *Nat. Commun.* **2024**, *15*, 1711.

[134] Zhang, W. J.; Liu, J.; Jin, Z. Controlled preparation of cross-linked SnO_2 hollow nanotube networks for electrocatalytic CO_2 reduction. *ACS Appl. Nano Mater.* **2023**, *6*, 11802–11809.

[135] Li, X.; Jiang, X. X.; Kong, Y.; Sun, J. J.; Hu, Q.; Chai, X. Y.; Yang, H. P.; He, C. X. Interface engineering of a GaN/In_2O_3 heterostructure for highly efficient electrocatalytic CO_2 reduction to formate. *Chin. J. Catal.* **2023**, *50*, 314–323.

[136] Guo, W. J.; Zhou, A.; Cai, W. W.; Zhang, J. T. *In situ* embedded bismuth nanoparticles among highly porous carbon fibers for efficient carbon dioxide reduction. *Rare Met.* **2024**, *43*, 4312–4320.

[137] Song, D. W.; Zhang, S. P.; Ning, H.; Fei, X.; Wang, M. W.; Wang, X. S.; Wu, W. T.; Zhao, Q. S.; Li, Y. Z.; Wu, M. B. Self-supporting BiCu/carbon hybrid nanofiber membrane promotes efficient CO_2 electroreduction to formate. *Sci. China Mater.* **2024**, *67*, 788–795.

[138] He, C. Y.; Wang, S. Y.; Jiang, X. X.; Hu, Q.; Yang, H. P.; He, C. X. Bimetallic cobalt-copper nanoparticle-decorated hollow carbon nanofibers for efficient CO_2 electroreduction. *Front. Chem.* **2022**, *10*, 904241.

[139] Zhang, W. B.; Zeng, J. C.; Liu, H. G.; Shi, Z. P.; Tang, Y.; Gao, Q. S. Co_xNi_{1-x} nanoalloys on N-doped carbon nanofibers: Electronic regulation toward efficient electrochemical CO_2 reduction. *J. Catal.* **2019**, *372*, 277–286.

[140] Hao, J. C.; Zhu, H.; Li, Y. Z.; Liu, P. X.; Lu, S. L.; Duan, F.; Dong, W. F.; Lu, Y. Y.; Liu, T. X.; Du, M. L. Tuning the electronic structure of AuNi homogeneous solid-solution alloy with positively charged Ni center for highly selective electrochemical CO_2 reduction. *Chem. Eng. J.* **2021**, *404*, 126523.

[141] Hao, J. C.; Zhuang, Z. C.; Hao, J. C.; Cao, K. C.; Hu, Y. X.; Wu, W. B.; Lu, S. L.; Wang, C.; Zhang, N.; Wang, D. S. et al. Strain relaxation in metal alloy catalysts steers the product selectivity of electrocatalytic CO_2 reduction. *ACS Catal.* **2022**, *16*, 3251–3263.

[142] Wei, X. X.; Xiao, S. H.; Wu, R.; Zhu, Z. Z.; Zhao, L.; Li, Z.; Wang, J. J.; Chen, J. S.; Wei, Z. D. Activating COOH* intermediate by Ni/$Ni_3ZnC_{0.7}$ heterostructure in porous N-doped carbon nanofibers for boosting CO_2 electroreduction. *Appl. Catal. B: Environ.* **2022**, *302*, 120861.

[143] Zhang, J.; Guo, C. X.; Fang, S. S.; Zhao, X. T.; Li, L.; Jiang, H. Y.; Liu, Z. Y.; Fan, Z. Q.; Xu, W. G.; Xiao, J. P. et al. Accelerating electrochemical CO_2 reduction to multi-carbon products via asymmetric intermediate binding at confined nanointerfaces. *Nat. Commun.* **2023**, *14*, 1298.

[144] Zhong, M.; Tran, K.; Min, Y. M.; Wang, C. H.; Wang, Z. Y.; Dinh, C. T.; De Luna, P.; Yu, Z. Q.; Rasouli, A. S.; Brodersen, P. et al. Accelerated discovery of CO_2 electrocatalysts using active machine learning. *Nature,* **2020**, *581*, 178–183.

[145] Li, J.; Chen, W. D.; Wang, M.; Zhu, H. W. Self-supporting copper-based electrode by electrospinning for reduction of carbon dioxide to methane. *Energy Technol.* **2021**, *9*, 2100714.

[146] Qu, T.; Hu, J. X.; Dai, X.; Tan, Q.; Liu, Y.; Chen, Y. Z.; Guo, S. W.; Liu, Y. N. Electrospinning highly dispersed Ru nanoparticle-embedded carbon nanofibers boost CO_2 reduction in a H_2/CO_2 fuel cell. *ACS Appl. Mater. Interfaces* **2021**, *13*, 23523–23531.

[147] Wang, J.; Cheng, C.; Huang, B. L.; Cao, J. L.; Li, L. G.; Shao, Q.; Zhang, L.; Huang, X. Q. Grain-boundary-engineered La_2CuO_4 perovskite nanobamboos for efficient CO_2 reduction reaction. *Nano Lett.* **2021**, *21*, 980–987.

[148] Zhang, D.; Zhou, J.; Luo, Y.; Wang, Y.; Zhang, X. Y.; Chen, X.; Liu, T.; Ding, M. Y. Robust cobalt-free perovskite type electrospun nanofiber cathode for efficient electrochemical carbon dioxide reduction reaction. *J. Power Sources* **2023**, *587*, 233705.

[149] Ferreira, A. C.; Martinho, J. F.; Branco, J. B. Hydrogenation of CO_2 over cobalt-lanthanide bimetallic oxide nanofibers. *ChemCatChem* **2022**, *14*, e202101548.

[150] Jiang, X. X.; Li, X.; Kong, Y.; Deng, C.; Li, X. J.; Hu, Q.; Yang, H. P.; He, C. X. A hierarchically structured tin-cobalt composite with an enhanced electronic effect for high-performance CO_2 electroreduction in a wide potential range. *J. Energy Chem.* **2023**, *76*, 462–469.

[151] Akhmadjonov, A.; Bae, K. T.; Lee, K. T. Novel perovskite oxide hybrid nanofibers embedded with nanocatalysts for highly efficient and durable electrodes in direct CO_2 electrolysis. *Nano-Micro Lett.* **2024**, *16*, 93.

[152] Zong, X.; Jing, Y. M.; Li, Y. M.; Zhang, X. B.; Zhang, S. J.; Xie, H. J.; Zhang, J. Q.; Xiong, Y. P. Morphology-controllable ZnO catalysts enriched with oxygen-vacancies for boosting CO_2 electroreduction to CO. *J. CO_2 Util.* **2022**, *61*, 102051.

[153] Sun, S. L.; Cheng, H. Y.; Li, X. C.; Wu, X. M.; Zhen, D. X.; Wang, Y. Q.; Jin, R.; He, G. H. Improving CO_2 electroreduction activity by creating an oxygen vacancy-rich surface with one-dimensional In-SnO_2 hollow nanofiber architecture. *Ind. Eng. Chem. Res.* **2021**, *60*, 1164–1174.

[154] Li, Y. M.; Jin, Y. M.; Zong, X.; Zhang, X. B.; Li, G. S.; Xiong, T. P. In-Bi bimetallic nanofibers with controllable crystal facets for high-rate electrochemical reduction of CO_2 to formate. *J. Mater. Chem. A* **2023**, *11*, 11445–11453.

[155] Li, H. J.; Huang, H. G.; Huang, W. S.; Zhang, X.; Hai, G. T.; Lai, F. L.; Zhu, T.; Bai, S. X.; Zhang, N.; Liu, T. X. Interfacial accumulation and stability enhancement effects triggered by built-in electric field of SnO_2/LaOCl nanofibers boost carbon dioxide electroreduction. *Small* **2024**, *20*, 2402654.

[156] Song, L. P.; Liang, Z.; Sun, M. Z.; Huang, B. L.; Du, Y. P. The interfacial effect induced by rare earth oxide in boosting the conversion of CO_2 to formate. *Energy Environ. Sci.* **2022**, *15*, 3494–3502.

[157] Al Harthi, A.; Al Abri, M.; Younus, H. A.; Al Hajri, R. Criteria and cutting-edge catalysts for CO_2 electrochemical reduction at the industrial scale. *J. CO_2 Util.* **2024**, *83*, 102819.

[158] He, C.; Xu, C.; Zhang, W. X. Instructive synergistic effect of coordinating phosphorus in transition-metal-doped β-phosphorus carbide guiding the design of high-performance CO_2RR electrocatalysts. *ACS Appl. Mater. Interfaces* **2023**, *15*, 57015–57028.

[159] Zhu, Q.; Gu, Y. T.; Wang, X. Z.; Gu, Y. M.; Ma, J. The Synergistic effect between metal and sulfur vacancy to boost CO_2 reduction efficiency: A study on descriptor transferability and activity prediction. *JACS Au* **2024**, *4*, 125–138.

[160] Bai, X. W.; Chen, C. J.; Zhao, X. H.; Zhang, Y. H.; Zheng, Y.; Jiao, Y. Accelerating the reaction kinetics of CO_2 reduction to multi-carbon products by synergistic effect between cation and aprotic solvent on copper electrodes. *Angew. Chem., Int. Ed.* **2024**, *63*, e202317512.